CHALMERS

Dynamic substructuring using experimental-analytical state-space models of automotive components

Master's thesis in Applied Mechanics

AXEL BYLIN

Department of Mechanics and Maritime Sciences
CHALMERS UNIVERSITY OF TECHNOLOGY
Göteborg, Sweden 2018

MASTER'S THESIS IN APPLIED MECHANICS

Dynamic substructuring using experimental-analytical state-space models of automotive components

AXEL BYLIN

Department of Mechanics and Maritime Sciences
Division of Dynamics
CHALMERS UNIVERSITY OF TECHNOLOGY

Göteborg, Sweden 2018

Dynamic substructuring using experimental-analytical state-space models of automotive components
AXEL BYLIN

Master's thesis 2018:69
Department of Mechanics and Maritime Sciences
Division of Dynamics
Chalmers University of Technology
SE-412 96 Göteborg
Sweden
Telephone: +46 (0)31-772 1000

Cover:
Body in white of the Volvo XC90 with its associated rear subframe

Chalmers Reproservice
Göteborg, Sweden 2018

Dynamic substructuring using experimental-analytical state-space models of automotive components
Master's thesis in Applied Mechanics
AXEL BYLIN
Department of Mechanics and Maritime Sciences
Division of Dynamics
Chalmers University of Technology

Abstract

Even though simulation models are getting better and better, thanks to both increased knowledge and computational powers, they are sometimes not perfect or not even good. Experimental models also have their drawbacks as they are often expensive and hard to obtain, to name a few. Within dynamic substructuring models of different components are coupled to get the dynamic response of the coupled system. Simulation models are typically finite element (FE) models and are denoted analytical models. The most common methods for coupling are best suited for either coupling of purely experimental, typically by frequency based substructuring, or purely analytical models, typically by component mode synthesis.

A coupling method based on state space models is however specifically developed to couple experimental models with analytical ditto. A successful implementation of the method, deeper understanding and highlighting of its advantages and drawbacks can thereby reduce the need for experimental models.

This report will describe the procedure of coupling an experimental model of a Volvo XC90 body-in-white with an analytical model of a rear subframe. Experimental modal analysis is performed to retrieve frequency response functions of the body-in-white. By system identification a state space model based on these are then coupled to a state space model of the subframe, based on FE data.

The resulting hybrid model, based on both experimental and analytical models, is then compared to both an experimental and an analytical model of the coupled system. Results are good, but to achieve good results the method put high demands on the used models.

Keywords: Substructuring, structural dynamics, system identification, modal analysis

Preface

This thesis is a collaberation between Chalmers University of Technology and Volvo Car Corporation. It is further related to an ongoing PhD project at Volvo Cars. In a structural dynamics course during the master program I came into contact with this area and found it very interesting

Acknowledgements

I would like to thank my supervisor Mladen Gibanica and examiner Thomas Abrahamsson for all support, help and initializing of this project. Your genuine interest in the project has been an asset in many ways.

Thanks to Volvo Cars and the people at the NVH department for support, help with simulations and resources for the measurements.

Lastly, I thank my girlfriend for all the support, especially during the writing of this thesis.

Contents

1 Introduction

In this thesis, dynamic substructuring has been used to couple an experimental model of a body-in-white (BIW) and an analytical model of a rear subframe. Both parts are from a Volvo XC90(2015) passenger car.

1.1 Background

Volvo Car Corporation (VCC) strives to reduce the amount of physical testing in favour of computer based simulations and models. These models are often accurate but there are examples where the are uncertain.

One component where large uncertainties have been seen is the BIW, in this case the Volvo XC90. In [4] experimental models, based on experimental modal analysis (EMA), and analytical models, finite element analysis (FEA) based, of this BIW are studied. Large differences were found between the models [4]. Since experimental models are seen as more truthful models, it is sometimes motivated to use these rather than the analytical models. The BIW is however a structure with complex dynamics that is hard to model also experimentally.

One interesting area of use, of these experimental models, is dynamic substructuring. This thesis will carry out the procedure of coupling an experimental model of the BIW with an analytical model of the rear subframe. On the contrary to the BIW the rear subframe is a component where good correlation between EMA and FEA has been found, specifically after model updating [6]. The coupling of these two structures are interesting as they are coupled through rubber bushings and the BIW is very dense with respect to the amount of modes.

In this thesis state space models are used for coupling. This particular coupling method was developed by Sjövall and AbraHamsson[13]. There are however other substructuring routines available such as frequency response function (FRF) based and component mode synthesis(CMS), de Klerk et al. [9] gives further information and references about these. These are however developed for coupling of experimental and analytical models, respectively.

The main advantage of substructuring is that large complex problems can be divided into smaller problems more easily modeled. As stated earlier it is also of interest to use computer based modeling as much as possible. By coupling state space models both analytical and experimental models can be used. One can thus use the best models availabe, regardless of what sources of information they are based on.

1.2 Purpose

The purpose of this thesis is to find how well substructuring with the specific state space approach,[13], can be applied to a BIW and rear subframe. The BIW will be modelled experimentaly and the rear subframe analyticaly. This way of coupling will be compared to coupling purely analytical models.

1.3 Limitations

The given FE model of the BIW is only supplied in a nominal version whereas the rear subframe is available as both a nominal and an updated version. For the experimental BIW and BIW rear subframe models, the measurements are done specifically for this project but the test setup, such as sensor placements, is similar to earlier studies of the same type of subframe and BIW.

1.4 Outline

The measurements took place at VCC where the BIW was measured both separately and with the subframe mounted. State space models of these two measurements were then identified and transformed such that coupling and comparisons could be done. The FE models of the subframe and the BIW were modified to suite the task, and were then exported and turned into state space models. After coupling of the models the results were compared.

A successful implementation of the method, deeper understanding and highlighting of its advantages and drawbacks can thereby reduce the need for experimental models.

2 Theory

This theory section describes several topics that are used to obtain experimental and analytical models and how to couple these in the state space domain.

2.1 Structural dynamics modeling

The analytical approach of structural dynamics modelling is explained below.

2.1.1 Second order form

A classical approach of the equations of motion (EOM) are

$$\boldsymbol{M}\ddot{\boldsymbol{q}}(t) + \boldsymbol{V}\dot{\boldsymbol{q}}(t) + \boldsymbol{K}\boldsymbol{q}(t) = \boldsymbol{f}(t). \tag{2.1}$$

The mass matrix $\boldsymbol{M}$, viscous damping matrix $\boldsymbol{V}$ and stiffness matrix $\boldsymbol{K}$ are all $N \times N$ symmetric matrices, where N is the number of degrees of freedom (DOF). $\boldsymbol{q}$ is the displacement vector and $\boldsymbol{f}$ the force vector, both are $N \times 1$ vectors. $\boldsymbol{M}, \boldsymbol{V}$ and $\boldsymbol{K}$ can be obtained in numerous ways. For simple systems Newtons laws or Lagranges equations are often used, especially for lumped systems. Industrial applications of larger models, typically continous systems, often uses the finite element method (FEM) to obtain $\boldsymbol{M}$ and $\boldsymbol{K}$. In these cases the damping $\boldsymbol{V}$ is approximated to be on a form such that $\boldsymbol{V}$ can be diagonalized by the systems undamped eigenmodes.

For the undamped problem the eigenmodes $\boldsymbol{\phi}_j$ and eigenvalue ω_j^2 are found by solving the equation

$$\left(\boldsymbol{K} - \omega_j^2 \boldsymbol{M}\right) \boldsymbol{\phi}_j = \boldsymbol{0}. \tag{2.2}$$

The eigenfrequency ω_j is expressed in rad/s. Further, the damping matrix $\boldsymbol{V}$ can then be written as

$$\boldsymbol{V} = \sum_{r=1}^{N} \frac{2\xi_r \omega_r}{M_r} \left(\boldsymbol{M}\boldsymbol{\phi}_r\right) \left(\boldsymbol{M}\boldsymbol{\phi}_r\right)^{\mathrm{T}} \tag{2.3}$$

where ξ_r is the damping and M_r is the modal mass of mode r defined as

$$M_r = \boldsymbol{\phi}_r \boldsymbol{M} \boldsymbol{\phi}_r^{\mathrm{T}}. \tag{2.4}$$

For more theory on this topic the reader is refered to [12].

2.1.2 Craig-Bampton Reduction

When the coefficient matrices $\boldsymbol{M}, \boldsymbol{V}$ and $\boldsymbol{K}$ come from a FE-model they are often large, say $N >> 10000$. The model gives N inputs and outputs but also N eigenmodes with corresponding eigenfrequencies (eigenvalues). In cases where output at all DOF or all eigenmodes is not desired, a reduction of the system may be convenient. In structural dynamics the modes occuring at the lowest frequencies are mostly of interest and usually only a few, relative to the total amount. A reduction with respect to number of modes and DOF is therefore wanted.

One reduction method is the Craig Bampton method [12] that is based on both fixed-interface normal modes and interface constraint modes. The fixed-interface normal modes, $\boldsymbol{\Phi}_{\mathrm{i}}$, are found by fixing all DOF that are interfacing other parts in a total assembly and solving the associated eigenvalue problem. If the stiffness and mass matrices are partitioned with the internal DOF first, subscript i, and the interface boundary DOF last, subscript b, the mode j can then be expressed

$$\{\boldsymbol{\Phi}_{\mathrm{i}}\}_j = \begin{bmatrix} \boldsymbol{\Phi}_{\mathrm{i}j} \\ \boldsymbol{0}_{\mathrm{b}j} \end{bmatrix} \quad \left(\boldsymbol{K} - \omega_j^2 \boldsymbol{M}\right) \{\boldsymbol{\Phi}_{\mathrm{i}}\}_j = \boldsymbol{0}. \tag{2.5}$$

The interface constraint modes, $\boldsymbol{\Psi}_{\mathrm{c}}$, are found by applying a unit displacement of the desired boundary coordinates, resulting in a static deformation as

$$\begin{bmatrix} \boldsymbol{K}_{\mathrm{ii}} & \boldsymbol{K}_{\mathrm{ib}} \\ \boldsymbol{K}_{\mathrm{bi}} & \boldsymbol{K}_{\mathrm{bb}} \end{bmatrix} \begin{bmatrix} \boldsymbol{\Psi}_{\mathrm{ib}} \\ \boldsymbol{I}_{\mathrm{bb}} \end{bmatrix} = \begin{bmatrix} \boldsymbol{0}_{\mathrm{ib}} \\ \boldsymbol{R}_{\mathrm{bb}} \end{bmatrix} \tag{2.6}$$

$$\boldsymbol{\Psi}_{\mathrm{c}} = \begin{bmatrix} \boldsymbol{\Psi}_{\mathrm{ib}} \\ \boldsymbol{I}_{\mathrm{bb}} \end{bmatrix} = \begin{bmatrix} -\boldsymbol{K}_{\mathrm{ii}}^{-1}\boldsymbol{K}_{\mathrm{ib}} \\ \boldsymbol{I}_{\mathrm{bb}} \end{bmatrix}. \tag{2.7}$$

Combining these two sets of modes gives the Craig Bampton transformation matrix

$$\boldsymbol{\Psi}_{\mathrm{CB}} = \begin{bmatrix} \boldsymbol{\Phi}_{\mathrm{i}k} & \boldsymbol{\Psi}_{\mathrm{ib}} \\ \boldsymbol{0} & \boldsymbol{I}_{\mathrm{bb}} \end{bmatrix}. \tag{2.8}$$

The displacements can be expressed by the use of this transformation matrix as

$$\begin{Bmatrix} \boldsymbol{q}_{\mathrm{i}} \\ \boldsymbol{q}_{\mathrm{b}} \end{Bmatrix} = \begin{bmatrix} \boldsymbol{\Phi}_{\mathrm{i}k} & \boldsymbol{\Psi}_{\mathrm{ib}} \\ \boldsymbol{0} & \boldsymbol{I}_{\mathrm{bb}} \end{bmatrix} \begin{Bmatrix} \hat{\boldsymbol{q}}_{k} \\ \boldsymbol{q}_{\mathrm{b}} \end{Bmatrix} \tag{2.9}$$

where it is important to notice that the boundary coordinates $\boldsymbol{q}_{\mathrm{b}}$ are not transformed. Transforming the mass and stiffness matrices gives

$$\hat{\boldsymbol{M}}_{\mathrm{CB}} = \boldsymbol{\Psi}_{\mathrm{CB}}^{-1}\boldsymbol{M}\boldsymbol{\Psi}_{\mathrm{CB}} = \begin{bmatrix} \boldsymbol{I}_{kk} & \hat{\boldsymbol{M}}_{k\mathrm{b}} \\ \hat{\boldsymbol{M}}_{\mathrm{b}k} & \hat{\boldsymbol{M}}_{\mathrm{bb}} \end{bmatrix}, \quad \hat{\boldsymbol{K}}_{\mathrm{CB}} = \boldsymbol{\Psi}_{\mathrm{CB}}^{-1}\boldsymbol{M}\boldsymbol{\Psi}_{\mathrm{CB}} = \begin{bmatrix} \boldsymbol{\Lambda}_{kk} & \boldsymbol{0}_{k\mathrm{b}} \\ \boldsymbol{0}_{\mathrm{b}k} & \boldsymbol{K}_{\mathrm{bb}} \end{bmatrix}. \tag{2.10}$$

2.1.3 State space form

In some applications it is necessary to rewrite the second order form of the equations of motion into a first order form. One way of doing this is to introduce the state space vector $\boldsymbol{x} = \begin{bmatrix}\boldsymbol{q}^T, & \dot{\boldsymbol{q}}^T\end{bmatrix}^T$. The external force vector $\boldsymbol{f}(t)$ is rewritten as $\boldsymbol{f}(t) = \boldsymbol{U}\boldsymbol{u}(t)$ were $\boldsymbol{u}(t)$ is a column vector with the inputs and $\boldsymbol{U}$ is a boolean matrix relating the input to a particular DOF.

$$\begin{bmatrix} \boldsymbol{V} & \boldsymbol{M} \\ \boldsymbol{I} & \boldsymbol{0} \end{bmatrix} \dot{\boldsymbol{x}} + \begin{bmatrix} \boldsymbol{K} & \boldsymbol{0} \\ \boldsymbol{0} & -\boldsymbol{I} \end{bmatrix} \boldsymbol{x} = \begin{bmatrix} \boldsymbol{U} \\ \boldsymbol{0} \end{bmatrix} \boldsymbol{u}(t) \tag{2.11}$$

After rearranging the terms $\dot{\boldsymbol{x}}$ can be expressed as

$$\dot{\boldsymbol{x}} = -\begin{bmatrix} \boldsymbol{V} & \boldsymbol{M} \\ \boldsymbol{I} & \boldsymbol{0} \end{bmatrix}^{-1} \begin{bmatrix} \boldsymbol{K} & \boldsymbol{0} \\ \boldsymbol{0} & -\boldsymbol{I} \end{bmatrix} \boldsymbol{x} + \begin{bmatrix} \boldsymbol{V} & \boldsymbol{M} \\ \boldsymbol{I} & \boldsymbol{0} \end{bmatrix}^{-1} \begin{bmatrix} \boldsymbol{U} \\ \boldsymbol{0} \end{bmatrix} \boldsymbol{u}(t) = \underbrace{\begin{bmatrix} \boldsymbol{0} & \boldsymbol{I} \\ -\boldsymbol{M}^{-1}\boldsymbol{K} & -\boldsymbol{M}^{-1}\boldsymbol{V} \end{bmatrix}}_{\boldsymbol{A}} \boldsymbol{x} + \underbrace{\begin{bmatrix} \boldsymbol{0} \\ \boldsymbol{M}^{-1}\boldsymbol{U} \end{bmatrix}}_{\boldsymbol{B}} \boldsymbol{u}(t). \tag{2.12}$$

The eigenvalues of $\boldsymbol{A}$ are generally complex valued where the imaginary part is the frequency of the mode and the real part relates to its damping. Each complex eigenvalue occurs in complex conjugate pairs.

It is further possible to relate the state vector $\boldsymbol{x}$ or its velocity $\dot{\boldsymbol{x}}$ to the wanted output. For receptance and mobility it is simply a boolean matrix multiplied by $\boldsymbol{x}$

$$\boldsymbol{y}_{\mathrm{d}} = \underbrace{\begin{bmatrix} \boldsymbol{P}_{\mathrm{d}} & \boldsymbol{0} \end{bmatrix}}_{\boldsymbol{C}_{\mathrm{d}}} \boldsymbol{x} \quad \text{and} \quad \boldsymbol{y}_{\mathrm{v}} = \underbrace{\begin{bmatrix} \boldsymbol{0} & \boldsymbol{P}_{\mathrm{v}} \end{bmatrix}}_{\boldsymbol{C}_{\mathrm{v}}} \boldsymbol{x}. \tag{2.13}$$

Since $\dot{\boldsymbol{y}}_{\mathrm{d}} = \boldsymbol{y}_{\mathrm{v}}$, a second expression for $\boldsymbol{y}_v$ is

$$\boldsymbol{y}_{\mathrm{v}} = \dot{\boldsymbol{y}}_{\mathrm{d}} = \boldsymbol{C}_{\mathrm{d}}\dot{\boldsymbol{x}} = \underbrace{\boldsymbol{C}_{\mathrm{d}}\boldsymbol{A}}_{\boldsymbol{C}_{\mathrm{v}}} \boldsymbol{x} + \underbrace{\boldsymbol{C}_{\mathrm{d}}\boldsymbol{B}}_{\boldsymbol{D}_{\mathrm{v}}} \boldsymbol{u} \tag{2.14}$$

In the velocity case the direct throughput from $\boldsymbol{u}$, and thus $\boldsymbol{D}_v$, is zero, due to Newton's second law $\boldsymbol{F} = m\boldsymbol{a}$. This implies that the receptance model has to fulfill $\boldsymbol{C}_{\mathrm{d}}\boldsymbol{B} = \boldsymbol{0}$ to ensure $\boldsymbol{D}_v = \boldsymbol{0}$.

To find accelerance, $\dot{\boldsymbol{x}}$ is used and is rewritten in terms of $\boldsymbol{x}$ and $\boldsymbol{u}$

$$\boldsymbol{y}_{\mathrm{a}} = \begin{bmatrix} \boldsymbol{0} & \boldsymbol{P}_{\mathrm{a}} \end{bmatrix} \dot{\boldsymbol{x}} = \underbrace{\begin{bmatrix} \boldsymbol{0} & \boldsymbol{P}_{\mathrm{a}} \end{bmatrix} \boldsymbol{A}}_{\boldsymbol{C}_{\mathrm{a}}} \boldsymbol{x} + \underbrace{\begin{bmatrix} \boldsymbol{0} & \boldsymbol{P}_{\mathrm{a}} \end{bmatrix} \boldsymbol{B}}_{\boldsymbol{D}_{\mathrm{a}}} \boldsymbol{u}. \tag{2.15}$$

The matrices $\boldsymbol{A}$, $\boldsymbol{B}$ and $\boldsymbol{C}$ are not uniquely defined as transformation of the state vector is possible.

2.2 State space system identification

In order to perform a state space system identification on data from vibrational measurements the data sometimes may need pre and post processing. Such processing may be required in order to make the final model describe the physics of the measured system, but also to make the inputs and outputs of the measured system match to the inputs and outputs of the desired model.

2.2.1 Virtual point transformation

Due to the geometry of the test object it is not always possible to place accelerometers as desired. Accelerometers can however be placed at arbitrary points located on parts that give quasi rigidly connections to the desired point of the output. The signals from such accelerometers can then be transformed to represent the rotation at any (virtual) point on that part. It can be shown that a minimum of six uni-axial accelerometers are needed to describe the translational and rotational motion of an arbitrary point that is rigidly connected to the accelerometers. Since tri-axial accelerometers are available the usage of these can reduce the amount of sensors. Using three tri-axial accelerometers gives an overdetermined transformation that can be solved in least square sense. One way of formulating this transformation is by the virtual point transformation [14].

By using this transformation not only translations at the desired outputs can be obtained but also rotations. For a tri axial accelerometer, with the output $\hat{\boldsymbol{y}}^k$, the motion $\boldsymbol{y}^v$ at the point v can be expressed as

$$\begin{Bmatrix} \hat{y}_x^k \\ \hat{y}_y^k \\ \hat{y}_z^k \end{Bmatrix} = \begin{bmatrix} e_{x,X}^k & e_{x,Y}^k & e_{x,Z}^k \\ e_{y,X}^k & e_{y,Y}^k & e_{y,Z}^k \\ e_{z,X}^k & e_{z,Y}^k & e_{z,Z}^k \end{bmatrix} \begin{bmatrix} 1 & 0 & 0 & 0 & r_Z^k & -r_Y^k \\ 0 & 1 & 0 & -r_Z^k & 0 & r_X^k \\ 0 & 0 & 1 & r_Y^k & -r_X^k & 0 \end{bmatrix} \begin{Bmatrix} y_X^v \\ y_Y^v \\ y_Z^v \\ y_{\Theta_X}^v \\ y_{\Theta_Y}^v \\ y_{\Theta_Z}^v \end{Bmatrix} \tag{2.16}$$

where r_i^k is the distance from the virtual point v to the position of sensor k in a global coordinate system. The left matrix is a transformation matrix from global coordinate system to the local system of the tri-axial accelerometers. This can also be expressed as

$$\hat{\boldsymbol{y}}^k = \boldsymbol{E}^{k^T} \overline{\boldsymbol{R}}^{kv} \boldsymbol{y}^v = \boldsymbol{R}^{kv} \boldsymbol{y}^v. \tag{2.17}$$

If one has n accelerometers the relation can be expressed as

$$\begin{Bmatrix} \hat{\boldsymbol{y}}^1 \\ \vdots \\ \hat{\boldsymbol{y}}^n \end{Bmatrix} = \begin{bmatrix} \boldsymbol{R}^{1v} \\ \vdots \\ \boldsymbol{R}^{nv} \end{bmatrix} \boldsymbol{y}^v \tag{2.18}$$

In a weighted least-square sense the transformation matrix from $\hat{\boldsymbol{y}}$ to $\boldsymbol{y}$ is thus

$$\boldsymbol{y} = \left(\boldsymbol{R}^T \boldsymbol{W} \boldsymbol{R}\right)^{-1} \boldsymbol{R}^T \boldsymbol{W} \boldsymbol{u} = \boldsymbol{T} \hat{\boldsymbol{y}} \tag{2.19}$$

where $\boldsymbol{W}$ is a weighting matrix. It is necessary that $\boldsymbol{R}$ is of full rank, thus a minimum of six outputs are needed. Worth mentioning is that two tri-axial accelerometers with six sensor outputs are not sufficient since rotation about an axis through the sensors cannot be captured, and would render $\boldsymbol{R}$ to be rank-deficient.

In a similar manner the inputs can also be transformed to the same virtual point. It will however not be used in this project but is explained in [14].

2.2.2 FRF

The frequency response function can be expressed both in terms of the state space and second order form using the Laplace transform

$$\mathcal{L}[x(t)] = X(s) = \int_0^\infty x(t) e^{-st} \mathrm{d}t. \tag{2.20}$$

If ones uses that $x(0) = 0$ the Laplace transform of equations 2.12-2.15 becomes

$$s\boldsymbol{X}(s) = \boldsymbol{A}\boldsymbol{X}(s) + \boldsymbol{B}\boldsymbol{U}(s) \tag{2.21}$$

$$\boldsymbol{Y}(s) = \boldsymbol{C}\boldsymbol{X}(s) + \boldsymbol{D}\boldsymbol{U}(s) \tag{2.22}$$

In the transfer function we have $s = j\omega$

$$\boldsymbol{H}(j\omega) = \frac{\boldsymbol{Y}(j\omega)}{\boldsymbol{U}(j\omega)} = \boldsymbol{C}\left(j\omega\mathbf{I} - \boldsymbol{A}\right)^{-1}\boldsymbol{B} + \boldsymbol{D} \tag{2.23}$$

2.2.3 N4SID

One common algorithm for obtaining a state space model of measured frequency response data is the N4SID algorithm [11]. The algorithm is implemented in MATLAB's system identification toolbox and gives the state space matrices $\boldsymbol{A}, \boldsymbol{B}, \boldsymbol{C}$ and $\boldsymbol{D}$ as output with input being FRF-data and the desired model order, i.e its number of states.

2.2.4 Residual states

One problem with the N4SID method is that for very modaly dense system with noise in the FRFs, it tends to identify noise modes within the measured frequency range, rather than residual modes outside that range. An accelerance FRF matrix of an undamped system with output j and input k can be written as

$$H_{jk}^{\mathrm{A}}(\omega) = \sum_{r=1}^{N} \frac{R_{jk}^{(r)}\omega^2}{\omega^2 - \omega_r^2} = \sum_{r=1}^{n_1-1} \frac{R_{jk}^{(r)}\omega^2}{\omega^2 - \omega_r^2} + \sum_{r=n_1}^{n_2} \frac{R_{jk}^{(r)}\omega^2}{\omega^2 - \omega_r^2} + \sum_{r=n_2+1}^{N} \frac{R_{jk}^{(r)}\omega^2}{\omega^2 - \omega_r^2}. \tag{2.24}$$

Where n_1 and n_2 gives the frequency range of the desired model and N is the total amount of states of the system. These residual terms constitute the first and two last sums of this series, and can be approximated as

$$H_{jk}^{\mathrm{A}}(\omega) \approx \frac{1}{M_{jk}^{(R)}} + \sum_{r=n_1}^{n_2} \frac{R_{jk}^{(r)}\omega^2}{\omega^2 - \omega_r^2} + \frac{R_{jk}^{(S)}\omega^2}{\omega^2 - \omega_S^2} + \frac{R_{jk}^{(K)}\omega^2}{\omega^2 - \omega_K^2} \tag{2.25}$$

according to [7]. For FRFs from measurements in the interval $[\underline{\omega}, \overline{\omega}]$ Ref. [7] gives that ω_S can be set to $1.4279\overline{\omega}$. However, if one knows the frequency of a strong mode above $\overline{\omega}$, then this frequency is another candidate for ω_S. The last residual state ω_K is typically placed high up in frequency range, approximately at $100\overline{\omega}$.

These residual states are then subtracted from the measured FRFs where system identification then can be made. The obtained state space model can then be superimposed to a state space model of the residual states. Thus the final model both contains states within the frequency range but also the effect of the states situated outside of the frequency range of the measured data.

2.2.5 Reciprocity

A structural dynamics system of the type presented in section 2.1 is a self-adjoint linear system. Systems of this type are reciprocal (Betti's Reciprocity Theorem), meaning that an input output relation of two points at the system is symmetrical $\boldsymbol{H}_{ij}(\omega) = \boldsymbol{H}_{ji}(\omega)$. It's also equivalent to $\boldsymbol{u}_1\boldsymbol{q}_2 = \boldsymbol{u}_2\boldsymbol{q}_1$ for energy conjugate generalized forces $\boldsymbol{u}_i$ and generalized displacements $\boldsymbol{q}_i$.

2.2.6 Superposition of state space models

State space models can easily be superimposed. For the special case where superimposed systems contains the same inputs and outputs, $\boldsymbol{u}_1 = \boldsymbol{u}_2$ and $\boldsymbol{y}_1 = \boldsymbol{y}_2$,

$$\dot{\boldsymbol{x}} = \begin{bmatrix} \boldsymbol{A}_1 & \boldsymbol{0} \\ \boldsymbol{0} & \boldsymbol{A}_2 \end{bmatrix} \boldsymbol{x} + \begin{bmatrix} \boldsymbol{B}_1 \\ \boldsymbol{B}_2 \end{bmatrix} \boldsymbol{u} \tag{2.26}$$

$$\boldsymbol{y} = \begin{bmatrix} \boldsymbol{C}_1 & \boldsymbol{C}_2 \end{bmatrix} \boldsymbol{x} + \left(\boldsymbol{D}_1 + \boldsymbol{D}_2\right)\boldsymbol{u} \tag{2.27}$$

It can be shown that the eigenmodes and eigenfrequencies are preserved by this operation.

2.2.7 Reestimation of input and output matrices

After superposition of state space models the response from the states of the superimposed systems may effect each other. One case is when system identification is done on subsets of the total frequency interval. The response from one of the models then affects also the response outside of the frequency interval that it is modeling. Therefore a reestimation of $\boldsymbol{B}, \boldsymbol{C}$ and $\boldsymbol{D}$ can be necessary. One way of doing this is in least square sense. If one also would like to imply the physical constraint $\boldsymbol{CB} = \mathbf{0}$ these two sets of equations can be stated as

$$\begin{bmatrix} \boldsymbol{C}\left(j\omega\mathbf{I} - \boldsymbol{A}\right)^{-1}\boldsymbol{B} \\ w_{CB}\boldsymbol{CB} \end{bmatrix} = \begin{bmatrix} \boldsymbol{H}^{\mathrm{R}} \\ \mathbf{0} \end{bmatrix}. \tag{2.28}$$

Here the frequency response function is expressed in terms of the state space matrices with the constraint that and $w_{CB}\boldsymbol{CB} = \mathbf{0}$ where w_{CB} is a weight. $\boldsymbol{H}^{\mathrm{R}}$ is the measured FRF of the receptance. By iteratively solving these equations for a fixed $\boldsymbol{A}$ and $\boldsymbol{B}$ respectively $\boldsymbol{A}$ and $\boldsymbol{C}$ a state space model fulfilling the constrains and usually a good fit to data is obtained. The iterative procedure is as

$$\boldsymbol{C}^{p+1} = \arg\min_{C} \left\| \begin{bmatrix} \boldsymbol{H}^{\mathrm{R}} & \mathbf{0} \end{bmatrix} - \boldsymbol{C}\left[\left(j\omega\mathbf{I} - \boldsymbol{A}\right)^{-1}\boldsymbol{B}^{p} \quad w_{CB}\boldsymbol{B}^{p} \right] \right\| \tag{2.29}$$

$$\boldsymbol{B}^{p+1} = \arg\min_{B} \left\| \begin{bmatrix} \boldsymbol{H}^{\mathrm{R}} \\ \mathbf{0} \end{bmatrix} - \begin{bmatrix} \boldsymbol{C}^{p+1}\left(j\omega\mathbf{I} - \boldsymbol{A}\right)^{-1} \\ w_{CB}\boldsymbol{C}^{p+1} \end{bmatrix} \boldsymbol{B}^{p} \right\|. \tag{2.30}$$

From the original state space system $\boldsymbol{B}^0$ and $\boldsymbol{C}^0$ are obtained and p is the iteration index.

2.3 Substructuring

Dynamic substructuring can be done in several ways. Except for coupling of state space models one can also couple FRFs and in the physical domain, these will however not be treated here but are described by Klerk et al. [9].

2.3.1 State space domain

The state space model based coupling procedure used in this report has been proposed by Sjövall and Abrahamsson[13]. The method builds on that the inputs and outputs are arranged by the coupling DOFs and the internal body DOFs.

$$\boldsymbol{y}^i = \begin{Bmatrix} \boldsymbol{y}^i_{\mathrm{c}} \\ \boldsymbol{y}^i_{\mathrm{b}} \end{Bmatrix}, \quad \boldsymbol{u}^i = \begin{Bmatrix} \boldsymbol{u}^i_{\mathrm{c}} \\ \boldsymbol{u}^i_{\mathrm{b}} \end{Bmatrix} \tag{2.31}$$

Arranging the coupling DOFs in the same order for both subsystem the response and excitation at the coupling can be written as

$$\begin{Bmatrix} \boldsymbol{y}^{\mathrm{I}}_{\mathrm{c}} \\ \boldsymbol{y}^{\mathrm{II}}_{\mathrm{c}} \end{Bmatrix} = \begin{bmatrix} \mathbf{I} \\ \mathbf{I} \end{bmatrix} \bar{\boldsymbol{y}}_{\mathrm{c}} \quad \text{and} \quad \bar{\boldsymbol{u}}_{c} = \begin{bmatrix} \mathbf{I} & \mathbf{I} \end{bmatrix} \begin{Bmatrix} \boldsymbol{u}^{\mathrm{I}}_{\mathrm{c}} \\ \boldsymbol{u}^{\mathrm{II}}_{\mathrm{c}} \end{Bmatrix} \tag{2.32}$$

Further a transformation is done of the original state vector $\boldsymbol{x}$ to the form

$$\tilde{\boldsymbol{x}}^i = \boldsymbol{T}^i\boldsymbol{x}^i = \begin{Bmatrix} \dot{\boldsymbol{y}}^i_{\mathrm{c}} \\ \boldsymbol{y}^i_{\mathrm{c}} \\ \boldsymbol{x}^i_{\mathrm{b}} \end{Bmatrix} \quad \boldsymbol{T} = \begin{bmatrix} \boldsymbol{C}_c\boldsymbol{A} \\ \boldsymbol{C}_c \\ \boldsymbol{\Psi}\mathbf{N}(\boldsymbol{B}_c) + \boldsymbol{Q}\boldsymbol{C}_d \end{bmatrix} = \begin{bmatrix} \boldsymbol{T}_1 \\ \boldsymbol{T}_2 \\ \boldsymbol{T}_3 \end{bmatrix} \tag{2.33}$$

The partition of $\boldsymbol{C}$ pertinent to output at the coupling dofs is denoted $\boldsymbol{C}_c$. Here, $\boldsymbol{\Psi}$ can be chosen arbitrary but must be such that $\boldsymbol{T}$ is non-singular, such that $\boldsymbol{Z} = \begin{bmatrix} \boldsymbol{Z}_1 & \boldsymbol{Z}_2 & \boldsymbol{Z}_3 \end{bmatrix} = \boldsymbol{T}^{-1}$. With $\boldsymbol{Q} = -\boldsymbol{\Psi}\mathbf{N}(\boldsymbol{B}_c)\boldsymbol{A}\boldsymbol{Z}_1$ the transformation matrix $\boldsymbol{T}$ transforms $\boldsymbol{A}$, $\boldsymbol{B}$ and $\boldsymbol{C}$ to

$$\tilde{\boldsymbol{A}}^i = \begin{bmatrix} \boldsymbol{A}^i_{\mathrm{vv}} & \boldsymbol{A}^i_{\mathrm{vd}} & \boldsymbol{A}^i_{\mathrm{vb}} \\ \mathbf{I} & \mathbf{0} & \mathbf{0} \\ \mathbf{0} & \boldsymbol{A}^i_{\mathrm{bd}} & \boldsymbol{A}^i_{\mathrm{bb}} \end{bmatrix}, \quad \tilde{\boldsymbol{B}}^i = \begin{bmatrix} \boldsymbol{B}^i_{\mathrm{vv}} & \boldsymbol{B}^i_{\mathrm{vb}} \\ \mathbf{0} & \mathbf{0} \\ \mathbf{0} & \boldsymbol{B}^i_{\mathrm{bb}} \end{bmatrix}, \quad \tilde{\boldsymbol{C}}^i = \begin{bmatrix} \mathbf{0} & \mathbf{I} & \mathbf{0} \\ \boldsymbol{C}^i_{\mathrm{bv}} & \boldsymbol{C}^i_{\mathrm{bd}} & \boldsymbol{C}^i_{\mathrm{bb}} \end{bmatrix}. \tag{2.34}$$

Writing the system on this form simplifies the introduction of the kinematic and equilibrium conditions at the coupling points. That is to prescribe the same displacement and velocity of the coupling nodes at both systems. The force equilibrium is enforced by writing

$$\boldsymbol{u}_{\mathrm{c}}^{\mathrm{I}} = \boldsymbol{u}_{\mathrm{c}}^{\mathrm{I,II}} + \boldsymbol{u}_{\mathrm{c,e}}^{\mathrm{I}}, \quad \boldsymbol{u}_{\mathrm{c}}^{\mathrm{II}} = -\boldsymbol{u}_{\mathrm{c}}^{\mathrm{I,II}} + \boldsymbol{u}_{\mathrm{c,e}}^{\mathrm{II}}. \tag{2.35}$$

Here, $\boldsymbol{u}_{\mathrm{c}}^{\mathrm{I,II}}$ is the cross sectional forces between the components and $\boldsymbol{u}_{\mathrm{c,e}}^{i}$ is the externally applied forces at the coupling dofs. The coupled system is then written as

$$\begin{Bmatrix} \ddot{\boldsymbol{y}}_{\mathrm{c}} \\ \dot{\boldsymbol{y}}_{\mathrm{c}} \\ \dot{\boldsymbol{x}}_{\mathrm{b}}^{\mathrm{I}} \\ \dot{\boldsymbol{x}}_{\mathrm{b}}^{\mathrm{II}} \end{Bmatrix} = \begin{bmatrix} \bar{\boldsymbol{A}}_{\mathrm{vv}} & \bar{\boldsymbol{A}}_{\mathrm{vd}} & \bar{\boldsymbol{A}}_{\mathrm{vb}}^{\mathrm{I}} & \bar{\boldsymbol{A}}_{\mathrm{vb}}^{\mathrm{II}} \\ \mathbf{I} & \mathbf{0} & \mathbf{0} & \mathbf{0} \\ \mathbf{0} & \boldsymbol{A}_{\mathrm{bd}}^{\mathrm{I}} & \boldsymbol{A}_{\mathrm{bb}}^{\mathrm{I}} & \mathbf{0} \\ \mathbf{0} & \boldsymbol{A}_{\mathrm{bd}}^{\mathrm{II}} & \mathbf{0} & \boldsymbol{A}_{\mathrm{bb}}^{\mathrm{II}} \end{bmatrix} \begin{Bmatrix} \dot{\bar{\boldsymbol{y}}}_{\mathrm{c}} \\ \bar{\boldsymbol{y}}_{\mathrm{c}} \\ \boldsymbol{x}_{\mathrm{b}}^{\mathrm{I}} \\ \boldsymbol{x}_{\mathrm{b}}^{\mathrm{II}} \end{Bmatrix} + \begin{bmatrix} \bar{\boldsymbol{B}}_{\mathrm{v}} & \bar{\boldsymbol{B}}_{\mathrm{vb}}^{\mathrm{I}} & \bar{\boldsymbol{B}}_{\mathrm{vb}}^{\mathrm{II}} \\ \mathbf{0} & \mathbf{0} & \mathbf{0} \\ \mathbf{0} & \boldsymbol{B}_{\mathrm{bb}}^{\mathrm{I}} & \mathbf{0} \\ \mathbf{0} & \mathbf{0} & \boldsymbol{B}_{\mathrm{bb}}^{\mathrm{II}} \end{bmatrix} \begin{Bmatrix} \bar{\boldsymbol{u}}_{\mathrm{c}} \\ \boldsymbol{u}_{\mathrm{b}} \\ \boldsymbol{u}_{\mathrm{b}} \end{Bmatrix} \tag{2.36}$$

$$\begin{Bmatrix} \bar{\boldsymbol{y}}_{\mathrm{c}} \\ \boldsymbol{x}_{\mathrm{b}}^{\mathrm{I}} \\ \boldsymbol{x}_{\mathrm{b}}^{\mathrm{II}} \end{Bmatrix} = \begin{bmatrix} \mathbf{0} & \mathbf{I} & \mathbf{0} & \mathbf{0} \\ \boldsymbol{C}_{\mathrm{bv}}^{\mathrm{I}} & \boldsymbol{C}_{\mathrm{bd}}^{\mathrm{I}} & \boldsymbol{C}_{\mathrm{bb}}^{\mathrm{I}} & \mathbf{0} \\ \boldsymbol{C}_{\mathrm{bv}}^{\mathrm{II}} & \boldsymbol{C}_{\mathrm{bd}}^{\mathrm{II}} & \mathbf{0} & \boldsymbol{C}_{\mathrm{bb}}^{\mathrm{II}} \end{bmatrix} \begin{Bmatrix} \dot{\bar{\boldsymbol{y}}}_{\mathrm{c}} \\ \bar{\boldsymbol{y}}_{\mathrm{c}} \\ \boldsymbol{x}_{\mathrm{b}}^{\mathrm{I}} \\ \boldsymbol{x}_{\mathrm{b}}^{\mathrm{II}} \end{Bmatrix} \tag{2.37}$$

with

$$\begin{aligned} \boldsymbol{K} &= \left(\boldsymbol{B}_{\mathrm{v}}^{\mathrm{I}} + \boldsymbol{B}_{\mathrm{v}}^{\mathrm{II}}\right)^{-1} \\ \bar{\boldsymbol{A}}_{\mathrm{vv}} &= \boldsymbol{B}_{\mathrm{vv}}^{I}\boldsymbol{K}\boldsymbol{A}_{\mathrm{vv}}^{II} + \boldsymbol{B}_{\mathrm{vv}}^{II}\boldsymbol{K}\boldsymbol{A}_{\mathrm{vv}}^{I} \\ \bar{\boldsymbol{A}}_{\mathrm{vd}} &= \boldsymbol{B}_{\mathrm{vv}}^{I}\boldsymbol{K}\boldsymbol{A}_{\mathrm{vd}}^{II} + \boldsymbol{B}_{\mathrm{vv}}^{II}\boldsymbol{K}\boldsymbol{A}_{\mathrm{vd}}^{I} \\ \bar{\boldsymbol{A}}_{\mathrm{vb}}^{I} &= \boldsymbol{B}_{\mathrm{vv}}^{II}\boldsymbol{K}\boldsymbol{A}_{\mathrm{vb}}^{I} \\ \bar{\boldsymbol{A}}_{\mathrm{vb}}^{II} &= \boldsymbol{B}_{\mathrm{vv}}^{I}\boldsymbol{K}\boldsymbol{A}_{\mathrm{vb}}^{II} . \\ \bar{\boldsymbol{B}}_{\mathrm{vv}} &= \boldsymbol{B}_{\mathrm{vv}}^{I}\boldsymbol{K}\boldsymbol{A}_{vd}^{II} \\ \bar{\boldsymbol{B}}_{\mathrm{vb}}^{I} &= \boldsymbol{B}_{\mathrm{vv}}^{II}\boldsymbol{K}\boldsymbol{A}_{\mathrm{vb}}^{I} \\ \bar{\boldsymbol{B}}_{\mathrm{vb}}^{II} &= \boldsymbol{B}_{\mathrm{vv}}^{I}\boldsymbol{K}\boldsymbol{A}_{\mathrm{vb}}^{II} \end{aligned} \tag{2.38}$$

It is of highest importance that the models fulfill the physical constraints $\boldsymbol{D} = \mathbf{0}$ and $\boldsymbol{CB} = \mathbf{0}$. Also, $\boldsymbol{CB} = \mathbf{0}$ is essential for the transformed matrices to be on the right form and $\boldsymbol{D} = \mathbf{0}$ is used in the coupling procedure.

2.3.2 Passivity

In earlier applications of the presented coupling procedure of state space models passivity has been proved to be essential, in order for the coupled system to be stable [10]. This constraint is not addressed in this project.

2.3.3 Non excited interfaces

In order to fully perform the coupling procedure, all translation and rotation outputs and corresponding inputs must be available at the coupling points. If any input is missing in the test data it is however possible to find a model through a modal transformation, [1]. This transformation requires that the model fulfills reciprocity requirements. It is also important to highlight that the transformation only gives the corresponding input or output, thus one of them are needed to find the other one.

2.4 Correlation analysis

The state space model can easily be used for correlation analysis since its eigenmodes are easily obtained. The physical eigenmodes are simply found by solving the eigenvalue problem of $\boldsymbol{A}$ and multiplying its eigenvectors with $\boldsymbol{C}$.

2.4.1 MAC

A common effective correlation measurement, suitable for state space models, is the Modal Assurance Criterion,(MAC), [8]. It is based on the scalar product of the eigenvectors of the two models that are to be compared. The scalar product is normalized with respect to the vectors as

$$MAC(i,j) = \frac{\left(\left(\boldsymbol{v}_i^{(\mathrm{A})}\right)^T \boldsymbol{v}_j^{(\mathrm{X})}\right)^2}{|\boldsymbol{v}_i^{(\mathrm{A})}|^2 |\boldsymbol{v}_j^{(\mathrm{X})}|^2} \tag{2.39}$$

Since eigenvectors are orthogonal an ideal MAC matrix is equal to the identity matrix.

2.4.2 MOC

The Modal Observability Criterion, MOC, [15] has similarities to MAC but also weights the eigenmodes with the eigenvalue. That is two identical eigenmodes from two different models but with different eigenvalues will not result in perfect correlation, 1. Also for this method two ideal models of the same systems gives a MOC matrix equal to the identity matrix. MOC is based on the observability matrix expressed in a balanced and diagonal form. The ordinary observability matrix is defined as

$$\bar{\mathcal{O}}^{\mathrm{T}} = \begin{bmatrix} \boldsymbol{C}^{\mathrm{T}} & (\boldsymbol{CA})^{\mathrm{T}} & \dots & (\boldsymbol{CA}^{n-1})^{\mathrm{T}} \end{bmatrix}. \tag{2.40}$$

By the use of the $\boldsymbol{T}_1$ diagonalizing transformation and $\boldsymbol{T}_2$ balancing transformation we can use the transformed matrices $\bar{\boldsymbol{C}} = \boldsymbol{C}\boldsymbol{T}_1\boldsymbol{T}_2$ and $\bar{\boldsymbol{A}} = (\boldsymbol{T}_1\boldsymbol{T}_2)^{-1}\boldsymbol{A}\boldsymbol{T}_1\boldsymbol{T}_2$ such that each column of $\mathcal{O}$ is related to only one eigenmode

$$\mathcal{O}_i = \begin{bmatrix} \boldsymbol{C}\boldsymbol{\phi}_i T_2^{(i)} \\ \boldsymbol{C}\boldsymbol{\phi}_i T_2^{(i)} \lambda_i \\ \dots \\ \boldsymbol{C}\boldsymbol{\phi}_i T_2^{(i)} \lambda_i^{n-1} \end{bmatrix} \tag{2.41}$$

where $\boldsymbol{\phi}_i$ is the ith eigenmode of $\boldsymbol{A}$.

$$MOC(i,j) = \frac{\left|\left(\bar{\mathcal{O}}_i^{(\mathrm{A})}\right)^{\mathsf{H}} \left(\bar{\mathcal{O}}_i^{(\mathrm{X})}\right)\right|}{\max\left(\left(\bar{\mathcal{O}}_i^{(\mathrm{A})}\right)^{\mathsf{H}} \left(\bar{\mathcal{O}}_i^{(\mathrm{A})}\right), \left(\bar{\mathcal{O}}_i^{(\mathrm{X})}\right)^{\mathsf{H}} \left(\bar{\mathcal{O}}_i^{(\mathrm{X})}\right)\right)} \tag{2.42}$$

2.4.3 FRAC

The frequency response assurance criterion (FRAC) is somewhat similar to the MAC but instead of comparing modes the response for one channel over all frequencies are compared [8].

$$FRAC(i,j) = \frac{\left|\sum_{k=n}^{N} H_{i,j}^{(\mathrm{A})}(\omega_k) H_{i,j}^{(\mathrm{X})^{\mathsf{H}}}(\omega_k)\right|^2}{\sum_{k=n}^{N} \left|H_{i,j}^{(\mathrm{A})}(\omega_k)\right|^2 \sum_{k=n}^{N} \left|H_{i,j}^{(\mathrm{X})}(\omega_k)\right|^2} \tag{2.43}$$

The output is then the correlation for output i and input j between the analytical model, $H_{i,j}^{(\mathrm{A})}$, and experimental model, $H_{i,j}^{(\mathrm{X})}$. The sums ranges over the desired frequency range $\omega_k \in [\underline{\omega}, \overline{\omega}]$.

3 Method

The project can be divided into several subtasks that are all needed to achieve the coupled subframe and BIW system. Measurements, of both the combined system of BIW and subframe and only the BIW, are one of these. Further steps are FE simulations of the BIW and subframe. The obtained FE and experimental data were both used to obtain state space models of the subframe, the BIW and a combined system of both BIW and subframe.

3.1 Measurements

Two different constellations of test objects were measured in the project, but the same equipment was used for the measurements on all setups. The measurement system was a National Instruments PXI based system with the open source software AbraDAQ [5] as measurement software. Both triaxial and uniaxial accelerometers, Brüel & Kjaer 4524-B and 4507-B, together with a force transducer, Brüel & Kjaer 8203, were used to measure the vibrations of the specimen. The input force from the LDS V201 shaker, Brüel & Kjaer. Before the measurements a calibration check was made on all accelerometers.

The two test objects, the BIW and the subframe, are described independently below. Further are the two measurement setups desribed, both with BIW only and with the BIW together with its rear subframe.

3.1.1 BIW

The main test object was the BIW that had been retrieved from the Volvo Cars chassis factory. It was completely stripped down on removable parts except for front and rear bumper beams, and minor plastic parts mounted inside beams. It was retrieved from the factory at a stage were it can be seen as consisting of purely metal without additional damping or surface treatments. The BIW was placed on air inflated rubber cushions to get a suspension mimicking free-free boundary conditions. Figure 3.1a shows these rubber cushions and the BIW. Figure 3.1b shows the BIW in its whole.

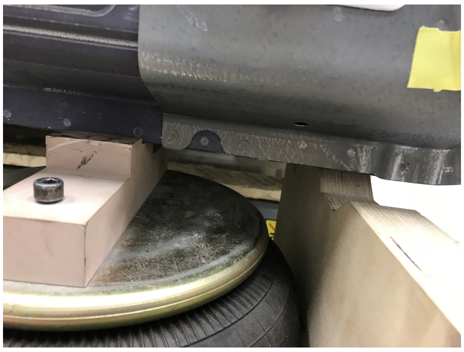

(a) *Figure of the BIW placed on the rubber suspension*

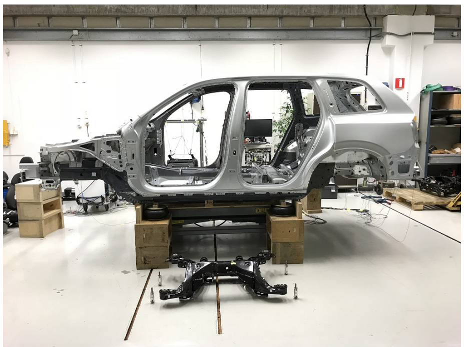

(b) *BIW on the support system with the a loose subframe placed in front*

Figure 3.1: *Figure of BIW, subframe and support system, photos courtesy of M. Gibanica.*

The vibrations of the BIW were measured with uniaxial accelerometers placed on the same positions as in earlier studies within VCC. In this way the data can be used in other studies and the measurement made earlier could be used as a reference. In figure 3.2 the positions of the accelerometers and the inputs are shown on a FE model of the BIW. Shown are also the virtual coupling points C1-C4 were the analytical subframe model is to be coupled.

The two input nodes, 21 and 22, were equipped with small threaded studs in addition to the accelerometers. The studs were glued with a strong epoxy glue such that the force transducer could safely be bolted to them. The force transducer was further connected to the shaker by a short (approximately 5 mm) and stiff metal stinger.

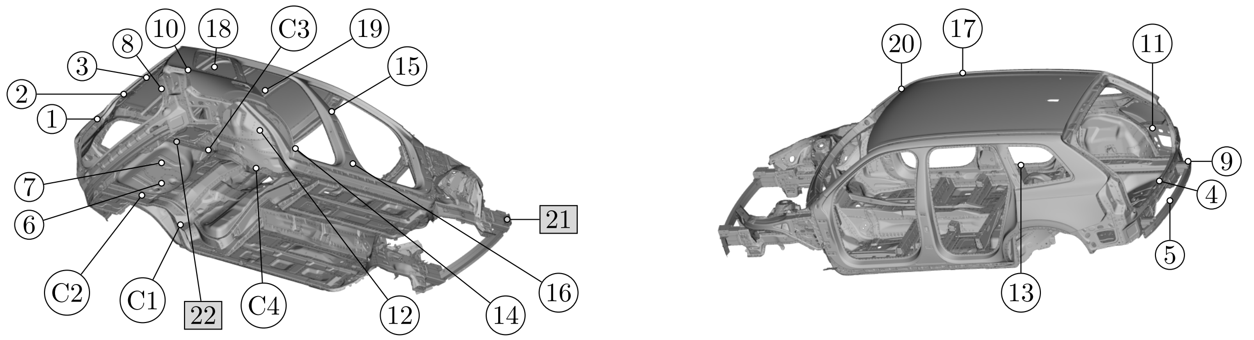

(a) *Rear bottom view* (b) *Side view*

Figure 3.2: *BIW with accelerometer and coupling points marked. Numbers within circles marks accelerometer, numbers within rectangles denotes accelerometer and force input. C1-C4 marks the coupling points. Figures from [2], by courtesy of M. Gibanica.*

(a) *Thread at accelerometer 21 where force transducer is mounted* (b) *Force input at accelerometer 21, photo courtesy of M. Gibanica* (c) *Force input at accelerometer 22*

Figure 3.3: *The two shaker inputs on the BIW.*

3.1.2 Rear subframe

The rear subframe was the second test object. It was of a final version with paint and bushings mounted. It is mounted to the BIW with a total of four bolts, one at each bushing placed on the four arms of the subframe. Ten triaxial and one uniaxial accelerometers were mounted on the subframe to measure the vibrations. Their positions can be seen in Figure 3.4.

At the uniaxial accelerometer a stud, identical to those on the BIW, had been mounted to get an input also on the subframe. The position of the triaxial accelerometers on the subframe were also reused from earlier studies [7].

3.1.3 Setup without subframe

The first measurement setup consisted of the BIW and four cylinders mounted on the same position as the subframe normally is mounted. Figure 3.5 shows the subframe and these aluminum cylinders. Virtual coupling points inside the subframes bushings and the corresponding point on the cylinders are marked.

The inner part of the bushings on the subframe arms is an aluminum cylinder. Simplified replicas of these were manufactured in aluminum. They were fitted with milled tracks were accelerometers could be placed. The height of the cylinder was 84mm with inner and outer radius 10.5mm and 17.6mm. They are very stiff in comparison to the surrounding thin sheet metal and can thereby be seen as rigid bodies.

Each cylinder was equipped with three triaxial accelerometers such that the motion of the rigid cylinders

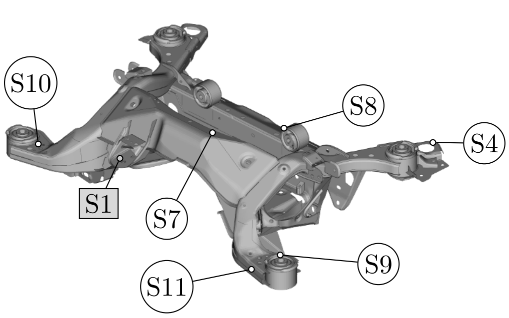

(a) *Top view*

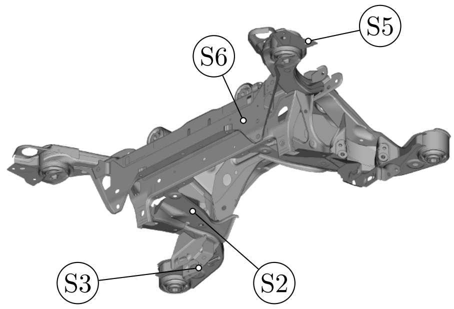

(b) *Bottom view*

Figure 3.4: *Subframe with positions of accelerometers marked, from [7]. Circle markings are triaxial accelerometers and the rectangular marking is a uniaxial accelerometer and input force position.*

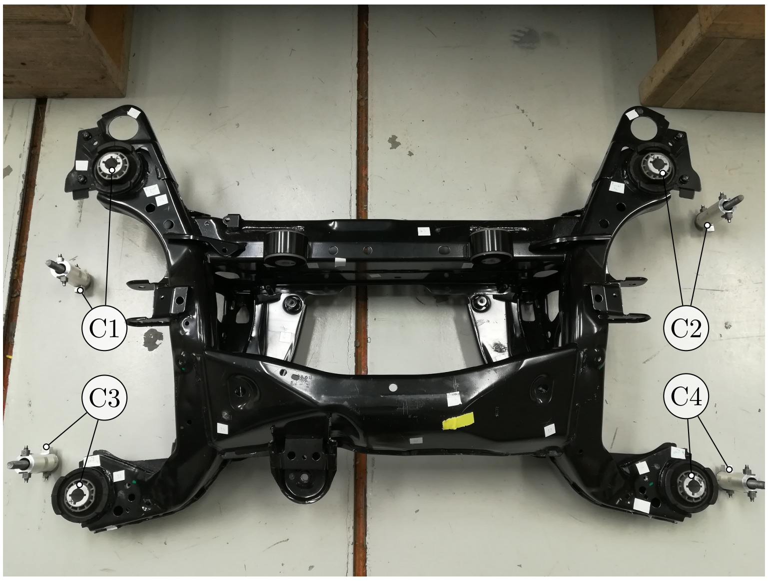

Figure 3.5: *Subframe from above with the virtual coupling points, C1-C4, marked both on subframe and cylinders*

could be fully described by the output of the accelerometers, and thus also the virtual coupling point. The accelerometers were mounted directly onto the tracks and aligned to within a few degrees degrees alignment error.

An aluminum cube, see Figure 3.6, was also mounted to each cylinder where three orthogonal surfaces had a small threaded hole. In these holes the force transducer could be bolted, resulting in three orthogonal force inputs at each cylinder. The holes were placed at the center of each surface such that the reversed normal at all holes were pointing to the center point of the cube. Detailed pictures of the cylinders and the positions of the accelerometers can be seen in the appendix, figure A.1.

For each of the 14 shaker inputs, twelve on the cylinders and two on the BIW, an identical measurement procedure was carried out. One stepped multisine stimulus with an amplitude of 1 N for the frequency interval 20 Hz − 300 Hz and 3 chirp signals, with amplitudes of 1, 2 and 3 N in the interval of 1 Hz − 500 Hz. Some slight dissonance could be heard at some of the 3 N chirp signal inputs. Two of the input locations on the cylinders can be seen in Figure 3.6.

Both the chirp and stepped multisine measurements were sampled with a frequency of 5 kHz. A total of 3000 frequency lines were used in the multisine measurement and 20 of these were superposed as the input signal at a time. The software stored averaged and stationary output signals for these frequencies. As for the chirp signal the frequency spectra was swept over a period of 20 s and repeated ten times and finally averaged. The reason for using both input signal types are that the multisine signal gives much less noise even for lower input amplitude. A drawback is, however, that it takes more than half an hour for one measurement with the settings used. This can be compared to the 200 s for one chirp measurement covering almost twice the

(a) *C1 with input in* $\boldsymbol{e}_x$ (b) *C1 with input in* $\boldsymbol{e}_z$

Figure 3.6: *C1 with two different inputs*

frequency range.

3.1.4 Setup with subframe

The second measurement setup consisted of the same BIW but with the aluminum cylinders replaced with the actual subframe. The subframe was fitted with ten triaxial and one uniaxial accelerometers. The same accelereometer and input positions on the BIW that were used on the earlier setup was used also here. The shaker signals were similar to that of the earlier measurements, four different input signals at the two input positions on the BIW and the one on the rear subframe.

3.2 Analytical models

Both an analytical FE-model of the rear subframe and the BIW was used in this project. Both FE-models were supplied by VCC and MSC Nastran was used as solver.

3.2.1 Rear subframe

The supplied model of the rear subframe was complete with appropriate mesh and two sets of material data. One nominal set and one with calibrated material data [6].

The model also included local coordinate systems at the accelerometer positions. These were used to get displacement output in the same direction as the accelerometers mounted on the subframe. The normal of all surfaces where defined as coinciding with the local z direction.

Since the measurements of the BIW also included the aluminum cylinders mounted at the coupling points their counterparts in the bushings had to be removed from the FE model of the subframe. Otherwise they would have been accounted for twice in the coupling. Rigid body elements (RBE2) were added to the surfaces were these cylinders had been fixed, such that the measured motion of the cylinders could be coupled to this surface. Dummy nodes were further added to the RBE2 elements. These nodes were placed, relatively to the removed cylinders, at the same position as the virtual coupling points. Figures 3.7a-3.7c illustrates one of the arms of the subframe and how the removed cylinder is replaced with an RBE2 element.

To create a state space model of the subframe its mass and stiffness matrices are needed. The mass and stiffness properties are only needed for the 55 DOFs were output and input is wanted and thus a Craig-Bampton reduction was used. The desired DOFs were X, Y, Z in local coordinates at each tri-axial accelerometer position, local Z at the uniaxial accelerometer/shaker input and both translational and rotational DOFs at the four

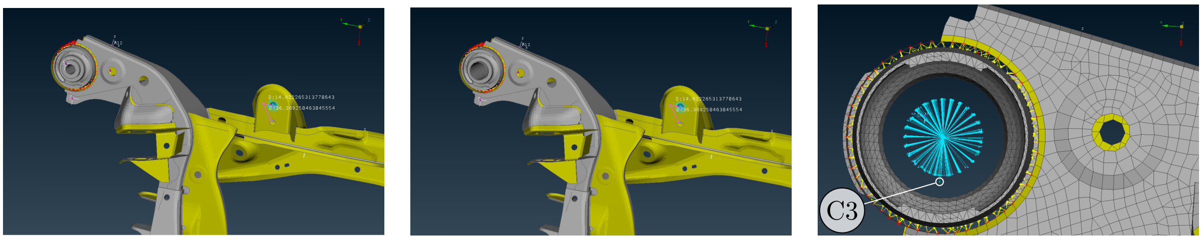

(a) *Figure of one of the arms of the subframe, without any modification*

(b) *Figure of one of the same arm as in figure 3.7a but with the inner cylinder of the bushing removed*

(c) *Figure of the same arm as in figure 3.7b but with some of the bushing parts hidden. In the middle is the added RBE2 element. In the bottom of it one can see the dummy node that has the same position as the center of the cube where inputs are applied*

Figure 3.7: *Figures of one of the subframes bushings and the virtual coupling point*

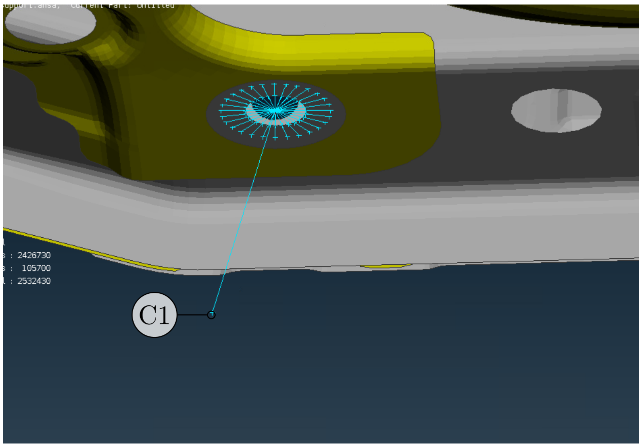

Figure 3.8: *C1 on the FE model of the BIW and how it is connected to the bolt hole were the subframe is mounted*

coupling points. An additional 66 fixed-interface modes were added to the 55 interface constraint modes thus resulting in mass and stiffness matrices with the size 121 × 121.

The mass and stiffness matrices were exported into a Nastran file of type op4 and imported into MATLAB. A state space model was then created according to section 2.1.3. The model had 55 outputs and 25 inputs, one at the shaker input and six at each coupling point. A 0.5 % damping was assigned to all modes of the nominal model. For the updated rear subframe model the identified modal damping was mapped to the identified modes of the model. For the remaining modes of the updated model the damping was set to 0.5 %

3.2.2 BIW

For the BIW only a nominal set of material data was available. Also here local coordinate systems were used at the accelerometer positions and RBE2 element were used at the coupling points, with a remote node at the same position as the input cube, see figure 3.8. This is a simplification as the mass of the cylinder is not modeled by this solution.

Unlike the free-free boundary conditions used for the rear subframe, soft springs were added to the BIW at the same positions as the support system in the measurements. These boundary conditions raised the rigid body modes from 0 Hz to mimic test conditions. A Craig Bampton reduction was also used with 46 DOFs and 406 interface constraint modes resulting in mass and stiffness matrices with the size 452 × 452.

A state space model based on the the mass and stiffness matrices and modal damping of 0.5 % could be made in MATLAB. A reduced version of the state space model was also made containing only the quasi-rigid body modes.

3.3 Experimental models

The procedure of converting the measured data to state space models consists of geometrical transformation of the measured data and then a system identification. To increase the quality of the model residual states were added outside of the frequency range. The identification was done on the multisine measurements on the frequency range $\omega = [\underline{\omega}, \overline{\omega}] = [30, 300]\,\mathrm{Hz}$. For the model based on data from BIW with cylinders a modal transformation was also performed on the identified system. The purpose of the transformation was to obtain torque inputs at the coupling DOFs.

3.3.1 Input and output transformation

In order to find the displacements and rotations at the virtual coupling points the output of the accelerometers on the cylinders had to be transformed. Transformation of the output was done according to section 2.2.1. For each cylinder a total of nine output signals were available, three signals from each of the three accelerometers, and the desired output consisted of six signals, three rotations and three translations. Thereby the transformation could either be done in a direct transformation by only using six of the output channels or in a least square sense by using seven, eight or nine of the output signals. The total amount of possible combinations where thereby 130 for each cylinder.

Due to symmetry, the two front cylinders had identical transformation matrices and the two back cylinders transformation matrices were also identical, both matrices only differed by sign at some of the elements. As a first attempt all cylinders were transformed with the same set of accelerometers. Figure 3.9 shows a schematic view of the two cylinders on the left side of the BIW. Figure 3.10 shows a similar view but for the subframe and the coupling cylinders. On the right side of the BIW the only difference is that the force applied normal to the view is of opposed sign.

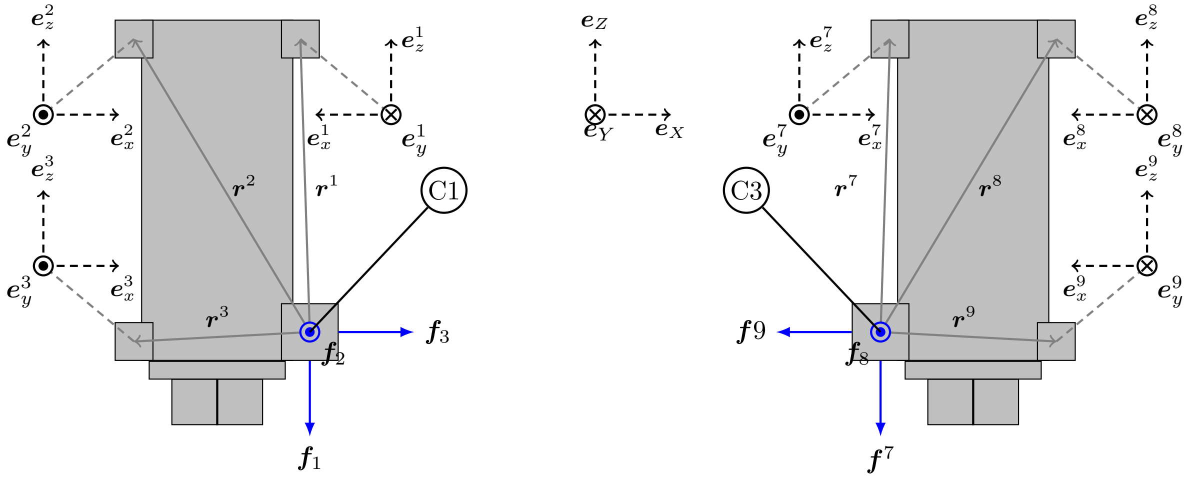

Figure 3.9: *Schematic view of the virtual points C1 and C3 with their corresponding cylinder, accelerometer and input forces*

By studying the condition number of the transformation matrices with respect to inversion, for all 130 possible transformation, good transformation candidates could be sorted out from bad ones. The condition number of the transformation matrix ranged from 188.43 to ∞ and the combination using all of the nine outputs resulted in a condition number of 203.53, see Table 3.1. T0 is the transformation using all channels, T1 is the optimum one with respect to the condition number and T2 is a special case for C3 when an outlier is taken into account, see further down.

There was no even spread between the condition numbers of the 130 configurations, instead they were clearly clustered. This can be seen in Table 3.2 where the number of combinations resulting in a condition number within the stated range is given. Common for the 33 transformations with lowest condition number was that they included all sensor channels in the $\boldsymbol{e}_y^i$ direction. The condition number however only takes the nominal position and orientation of the sensors into account. Noise and misalignment of sensors are thus not addressed as possible error sources.

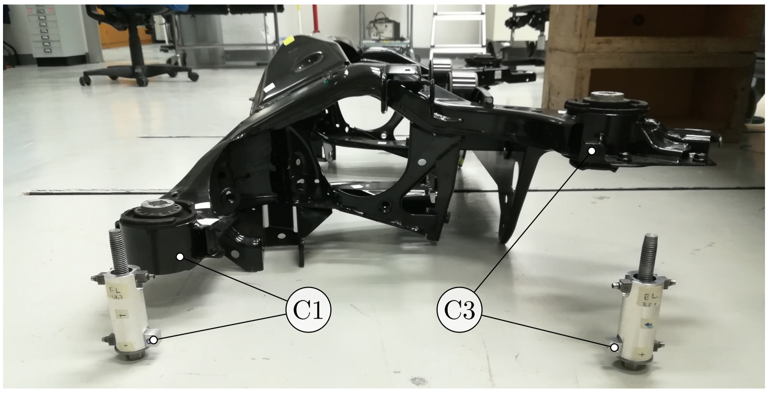

Figure 3.10: *View of the subframe and two of the cylinders with C1 and C3 marked*

Table 3.1: Table over the three geometrical transformation of specific interest and their corresponding condition number

	e_x^1	e_y^1	e_z^1	e_x^2	e_y^2	e_z^2	e_x^3	e_y^3	e_z^3	Cond
T0	X	X	X	X	X	-	X	X	-	188.43
T1	X	X	X	X	X	X	X	X	X	203.53
T2	X	X	X	X	X	X	-	X	X	311.64

The difference in condition number was seen as small and using more than the minimum six output channels assumingly diminish the effect of noise and possible frequency shift between sensors. As a first set of sensors all channels were used. The transformed data was compared to the optimum transformation, T1, and it was found that rotation in $\boldsymbol{e}_{\mathrm{Y}}$ changed significantly compared to the other channels, see figure 3.11. Especially cylinder three showed great variation for different transformations. The comparisons pointed out $\boldsymbol{e}_y^9$ as a possible reason for this non robustness and is a possible outlier.

Figure 3.12 shows the input in $\boldsymbol{e}_y$ on C3 for output in $\boldsymbol{e}_{\theta^Y}$ and $\boldsymbol{e}_{\theta^Z}$ on C3. The six different curves are obtained from the six different transformations using eight accelerometer channels when all $\boldsymbol{e}_y^i$ are used. In Figure 3.12b no difference is noticeable and this is representative for the rest of the channels. In Figure 3.12a the differences are big and the one where $\boldsymbol{e}_x^9$ is deficient and therefore its use was abandoned. It is therefore possible that this channels is somewhat faulty and was thus removed. On the other cylinders no similar behaviour was noticed and all channels were used in the transformation to the corresponding virtual coupling point.

As a further study of the sensitivity an angular misalignment of 0.5° in $\boldsymbol{e}^{\mathrm{Y}}$ was applied to each of the sensors. It was found to affect the output noticeable on all channels, see the result section.

The total transformation matrix has the form

$$\tilde{\boldsymbol{H}} = \begin{bmatrix} \boldsymbol{T}_1 & \boldsymbol{0} & \boldsymbol{0} & \boldsymbol{0} & \boldsymbol{0} \\ \boldsymbol{0} & \boldsymbol{T}_2 & \boldsymbol{0} & \boldsymbol{0} & \boldsymbol{0} \\ \boldsymbol{0} & \boldsymbol{0} & \boldsymbol{T}_3 & \boldsymbol{0} & \boldsymbol{0} \\ \boldsymbol{0} & \boldsymbol{0} & \boldsymbol{0} & \boldsymbol{T}_4 & \boldsymbol{0} \\ \boldsymbol{0} & \boldsymbol{0} & \boldsymbol{0} & \boldsymbol{0} & \mathbf{I} \end{bmatrix}_{out} \boldsymbol{H}\boldsymbol{T}_{in} = \boldsymbol{T}_{out}\boldsymbol{H}\boldsymbol{T}_{in} \tag{3.1}$$

where $\boldsymbol{T}_i$ is the local transformation matrix for the i:th virtual coupling point. $\boldsymbol{T}_{in}$ is a diagonal matrix with 1 and -1 corresponding to the orientation of the inputs. Since the input channels already were aligned with the virtual coupling point they only needed correction with respect to sign. For example $\boldsymbol{f}^9$ needs to be multiplied with -1 for the vector to point in positive $\boldsymbol{e}_X$.

Table 3.2: The spread of condition number of the different geometrical transformations

Range	188.43-203.53	295-335	900-1250	1700-10000	$10^{16} - \infty$
Number	24	9	24	23	50

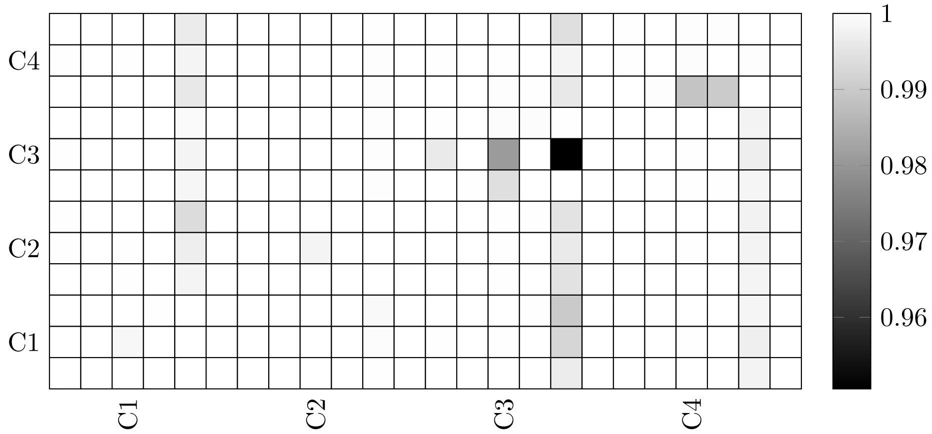

Figure 3.11: *Difference between T0 and T1 measured with the FRAC metric. The ordinate axis is for the three inputs for the four cylinders and the abscissa is the six outputs(translation and rotation) for the four cylinders*

3.3.2 System identification

The system identification was done in MATLAB using the N4SID algorithm on accelerance data where the influence of residual states had been removed. The reason for identifying on accelerance data, instead of receptance or mobility data, is that receptance and mobility data are rapidly decreasing with frequency which renders high-frequency modes less identifiable. Effects from low frequency residual modes were included as the BIW state space model of the quasi rigid body modes of the FE model. The high frequency residual effects were calculated according to section 2.2.4. The total frequency range was divided into subintervals before the system identification, to simplify the identification process.

Reciprocity

To ensure reciprocity of the system the FRAC was used between those points where both input and output data were available. It was found that the reciprocity from $\boldsymbol{e}_X$ to $\boldsymbol{e}_Y$ was poor for all cylinder except for number two, see figure 3.13a. On cylinder one also $\boldsymbol{e}_Y$ to $\boldsymbol{e}_Z$ were poor. Therefore reciprocal test data was obtained by averaging, i.e. data was set such that $\bar{\boldsymbol{H}}_{i,j} = \bar{\boldsymbol{H}}_{j,i} = \left(\boldsymbol{H}_{i,j} + \boldsymbol{H}_{j,i}\right)/2$.

Residual states

Since the vibration measurements were done in a limited frequency area residual states both below and above could be present. From a measurements with chirp data the rigid body modes can be seen to be in the area below 6Hz. The data was however very noisy and a reduced version of the FE BIW model was used instead, containing the six lowest eigenfrequencies. As upper limit residual states $\omega_S = 1.4279\bar{\omega}$ and $\omega_K = 100\bar{\omega}$ was used.

The method implies that one pair of complex conjugated modes should be added for each input at both frequencies. These states were slightly separated to avoid numerical problems with multiple eigenvalues. These numerical problems encountered when the $\boldsymbol{A}$ matrix was brought to a block diagonal form.

Identification

It was found that dividing the measured data into several frequency intervals that was identified separately increased the quality of the resulting model. Identifying on data for the entire frequency range at once took longer time, but more important caused that several distinct low frequency modes were left out. Attempts of doing the system identification on a partial system, subset of inputs and outputs, and then expand $\boldsymbol{B}$, $\boldsymbol{C}$ and $\boldsymbol{D}$ to include all inputs and outputs were also made. However, it was not found to increase the quality of the resulting model.

All identified systems were finally superposed together with the low and high frequency residual states systems. The desired output of the system is on receptance form and thus constraints needed to be imposed on $\boldsymbol{C}$ to render that the conditions $\boldsymbol{CB} = \boldsymbol{D} = \boldsymbol{0}$. By re-estimating $\boldsymbol{B}$ and $\boldsymbol{C}$, with $\boldsymbol{D} = \boldsymbol{0}$, with respect to

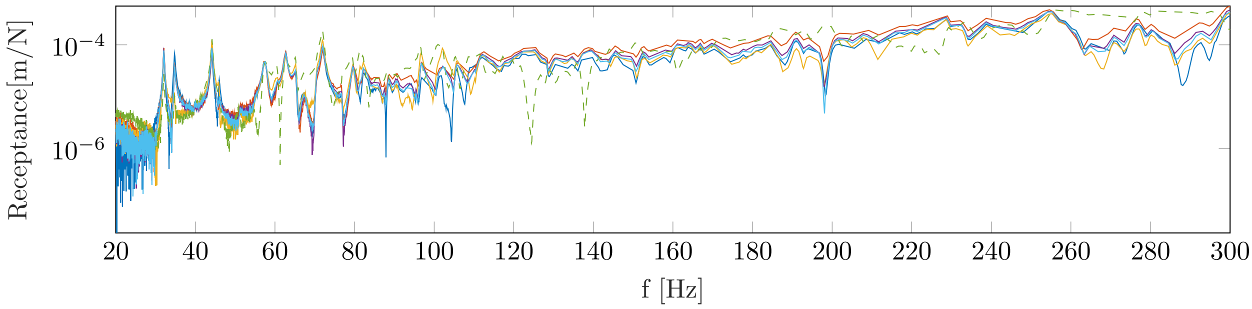

(a) *Input in e_Y on C3 with output $e_{\theta Y}$ for six different transformations. The dashed line is when data from $\boldsymbol{e}_x^9$ is not used*

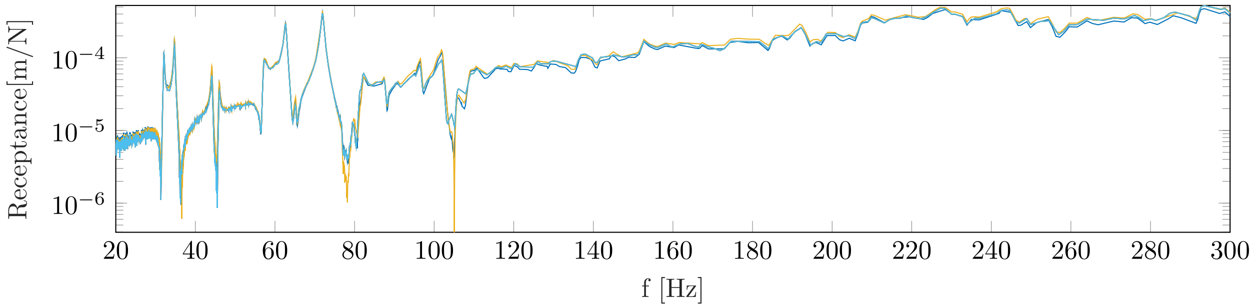

(b) *Input in e_Y on C3 with output $e_{\theta Z}$*

Figure 3.12: *Comparison between two channels where different sets of output channels are used to obtain the shown rotations*

data on receptance form this could be fulfilled. The reestimation of $\boldsymbol{B}$ and $\boldsymbol{C}$ was done iteratively according to section 2.2.7 and $\boldsymbol{D}$ was set strictly to zero.

3.3.3 Rotation inputs

Since only three force inputs were used at each virtual coupling point the torque inputs had to be retrieved by a modal transformation as in section 2.3.3.

A strong reciprocity is however necessary in order for the transformation to give good results. The identified models were close to fully reciprocal within the measured frequency interval but at the rigid body and high frequency residual states the reciprocity of the state-space models are poor. This comes from the re-estimation of $\boldsymbol{B}$ and $\boldsymbol{C}$ where the model is allowed to take any shape outside of the measured frequency interval. In figures 3.13b-3.13c the reciprocity is measured with FRAC for the measured frequency range and an extended interval including the low and high frequency states.

Comparing input and output of e^{X} and e^{Y} of C1 for the frequency intervals shows a large difference. These two channels are plotted in figure 3.14. As stated by figure 3.13b the reciprocity is good within the measured frequency interval but poor outside.

The resulting model from the modal transformation resulted in that the quality of several inputs and outputs were severely reduced. Instead of using this model directly, FRFs of the torque inputs were created and added to the data from measurement. They were however not added to those partitions of the FRF matrix that could be obtained by reciprocity, torque input and translation output at force inputs. An additional re-estimation of $\boldsymbol{B}$ and $\boldsymbol{C}$ gave a model that for force inputs was close to identical to the model from the system identification but also with torque inputs, although the quality of this part of the model was lower.

3.3.4 Coupling

The implementation of the coupling procedure according to 2.3.1 was done in MATLAB. Two FE based and two EMA based models of the BIW were used, in both cases one with only translational DOFs coupled and one with translation and rotation DoFs coupled. Also two subframe models were used, one nominal and one with updated parameters.

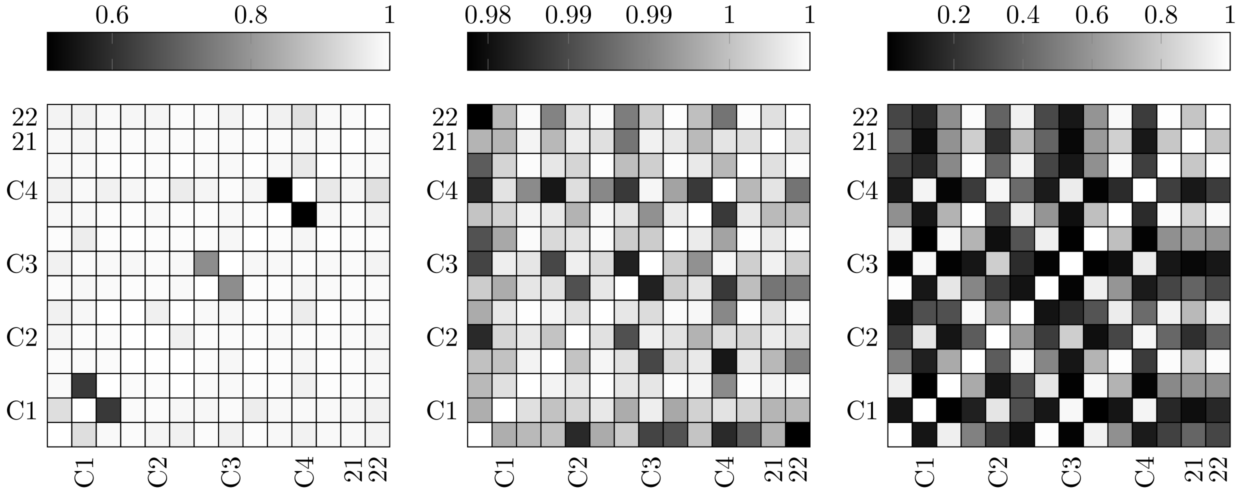

(a) *Reciprocity of the measured data according to FRAC*

(b) *Reciprocity of the identified model, within the measured frequency range, according to FRAC*

(c) *Reciprocity of the identified model, for the measured frequency range and the residual modes, according to FRAC*

Figure 3.13: *Reciprocity of measured data and identified model, the latter for two different frequency ranges*

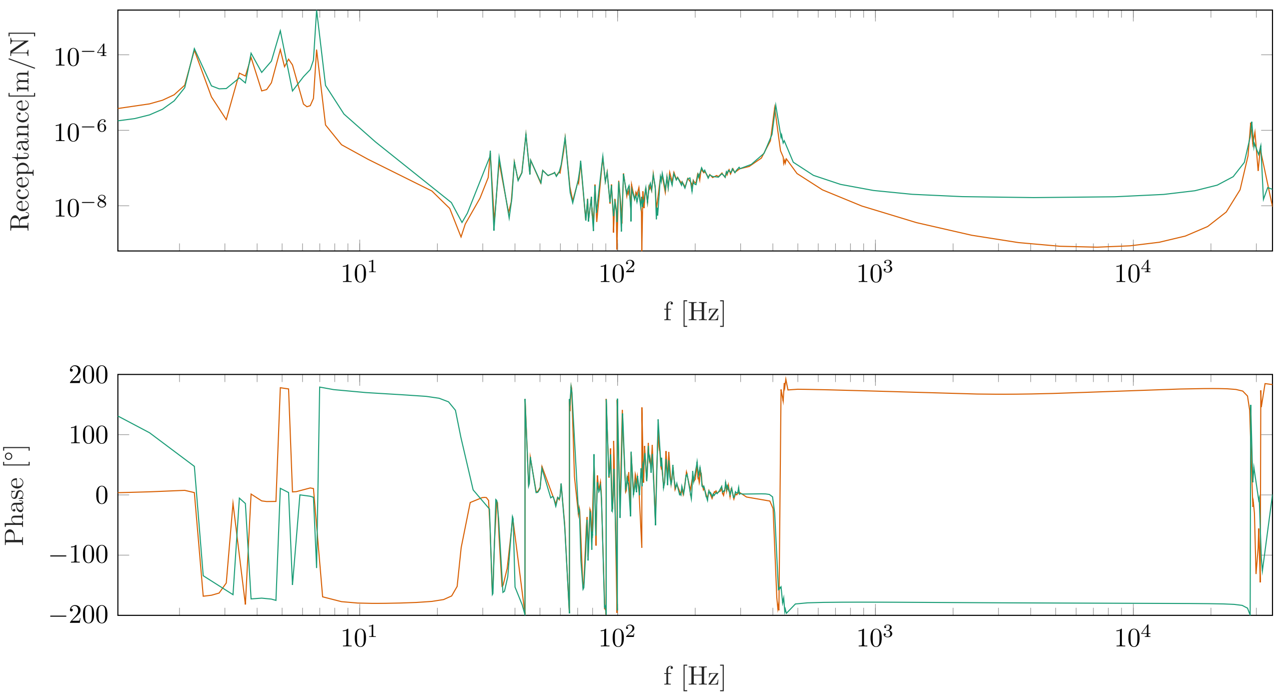

Figure 3.14: *Input in* $\boldsymbol{e}_X$ *and output in* $\boldsymbol{e}_Y$ *for C1 and its reciprocal response*

4 Results and discussion

The results regarding the outlined procedure in chapter 3 is presented and discussed below. Specifically the quality of the identified models and the correlation of the different coupled systems is presented and discussed.

4.1 System identification

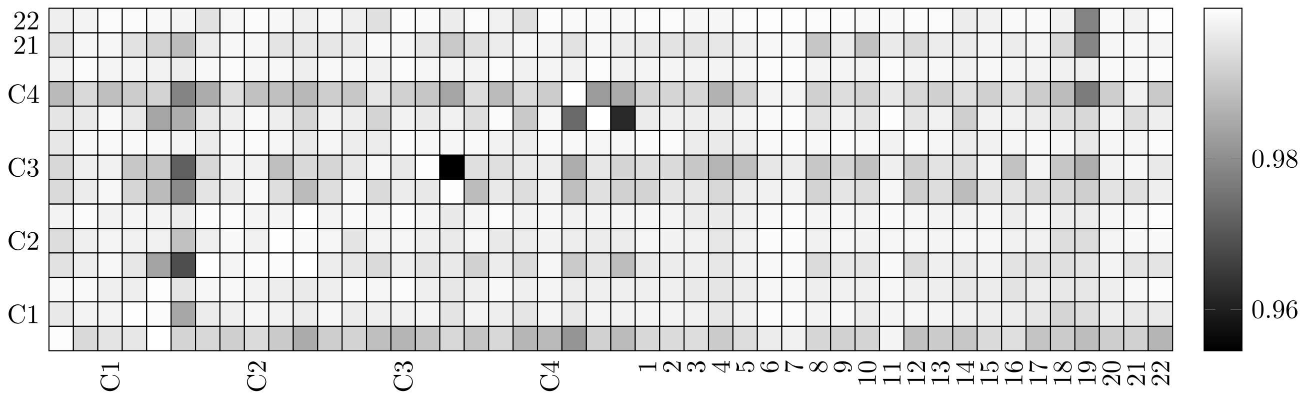

(a) *FRAC of the measured data and the identified system of the BIW with cylinders*

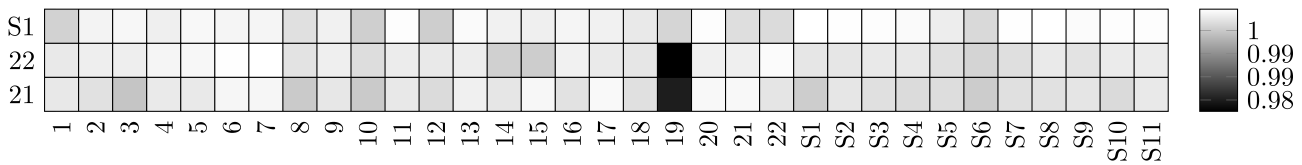

(b) *FRAC of the measured data and the identified system of the BIW and subframe*

Figure 4.1

The results from the system identification of the BIW and BIW with subframe measurements can bee seen in Figure 4.1. The FRAC between identified model and measured FRFs are presented. An overall good fit was obtained. However, some channels were noticeable worse than the rest, although still good with minimum FRAC at 0.955. In both figures output 19 stands out and some patterns can be found for the BIWs virtual coupling points. Some of the virtual point inputs gives lower fit to all outputs and rotation output in e^{Y} on C1 has good but noticeable lower fit to several inputs.

Ensuring that the model fulfills $\boldsymbol{CB} = 0$ was found to be of highest importance in the coupling procedure. The above results are for enforced $\boldsymbol{CB} = \boldsymbol{0}$.

4.2 Modal transformation

From the modal transformation the torque inputs were obtained. As can be seen in Figure 4.2a the fit to test data is reduced after the transformation. The re-estimation of $\boldsymbol{B}$ and $\boldsymbol{C}$ however gives a good fit to the extended test data, see Figure 4.2b except for the rotation input-output partitions. In the re-estimation one could have weighted these channels higher to ensure a better fit but it would have been on the cost of the other channels. However, since these channels are the most unsure it was not done.

The shortcomings from the modal transformation are due to the model being not fully reciprocal. Removing the residual states gave good results for the transformation. However, to achieve a good fit to test data the residual states are essential and no method of adding them after modal transformation for a reciprocal model including moment inputs was found during the course of this work.

An example of how poor the fit can be after the transformation can be seen in figure 4.3. The final re-estimated model has a good fit to test data but a poor fit directly after the transformation.

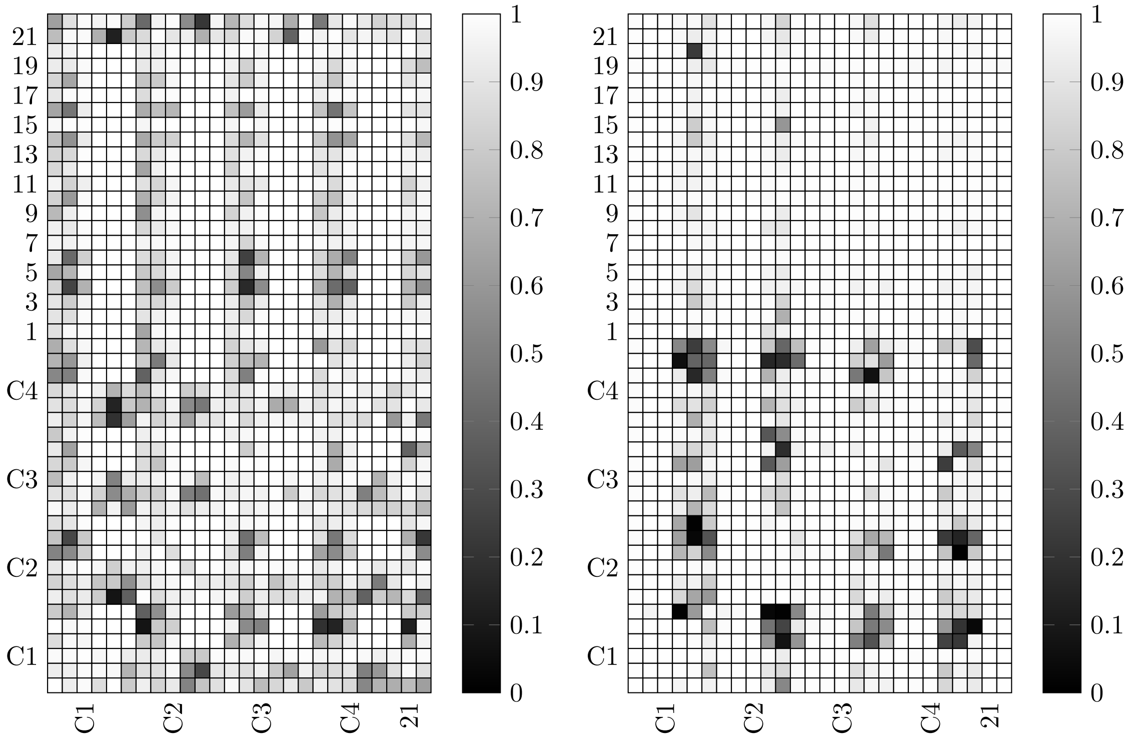

(a) *FRAC of the BIW model after transformation.* (b) *FRAC of the BIW model after transformation and reestimation of* $\boldsymbol{B}$ *and* $\boldsymbol{C}$

Figure 4.2

Implementation of reciprocity in the system identification is therefore a suggestion for future improvement as moment input to rotation output on the cylinders and moment input on cylinders and translation output on the BIW are very uncertain.

4.3 Coupling

A total of eight coupled systems were obtained based on two BIW models, one experimental and one analytical, and two subframe models, one nominal and one with calibrated material parameters. Each model combination was coupled in two ways, one with translations and one with both translations and rotations. In figure 4.4 the FRAC between the measured coupled system and the coupled state space models of the material parameter updated subframe.

The translation and rotation coupled system with the experimental BIW model is clearly superior to the other models. Transfer functions with inputs and outputs on the subframe show a poorer fit compared to transfer functions associated with the BIW. This, in particular regard the input on the subframe.

In Figure 4.4 the nominal subframe model is used and the model fit is significantly reduced for the experimental BIW model coupled with both translation and rotation, but also for the analytical. For the nominal models only coupled with translations the fit is to some extent improved. This could be due to the coupling with only translations is softer and the nominal subframe is stiffer, resulting in faults canceling each other.

The best and worst channel correlation according to Figure 4.4 are visualized in Figure 4.5-4.6 for the coupled models with the updated subframe. The fit is close to perfect for the experimental models up to 90 Hz and good for higher frequencies. The FE models still catch many of the modes gives significantly poorer results. For the models only coupled with translations spurious extra modes are present, for example at around 55 Hz for the experimental model. This is expected as each DOF constrained reduces the model by one eigenfrequency.

The MAC for the systems with updated subframe the analytical model is also better, see Figures 4.7a-4.7d. The matrix is clearly diagonal with only some cross correlation.

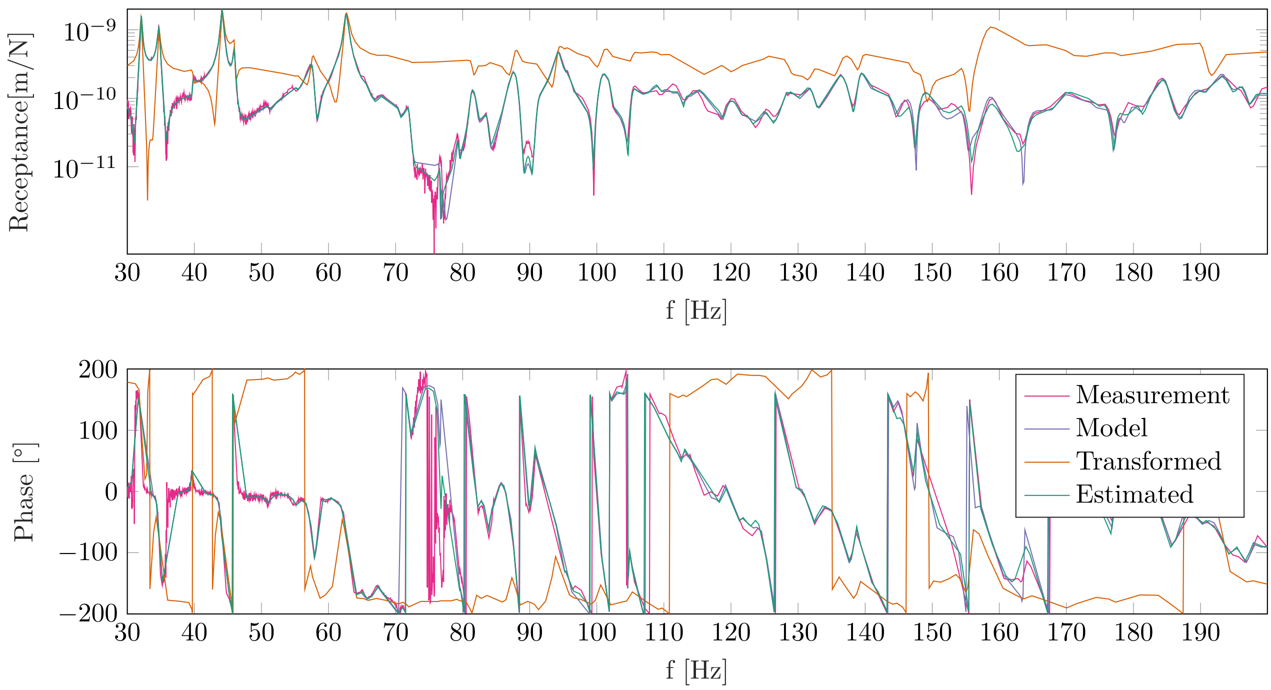

Figure 4.3: *Plot of input in $\boldsymbol{e}_Y$ on C1 with output in $\boldsymbol{e}_{\theta Y}$ on C2 for the measured data, the identified model, the model after modal transformation before(Transformed) and after reestimation of coefficient matrices(Estimated)*

The MAC for the nominal subframe, see figure 4.7e, is overall worse than the updated subframe. However, most of all a new low frequency modes is present and the fit to two of the low frequency modes is significantly reduced.

4.4 Further thoughts

The experimental setup used was found to be well suited for the task and no significant amounts of noise were measured. It was however found that the accelerometers on the cylinders were sensitive to angular misorientations. This can be seen in Figure 4.8. No channels are changed beyond recognition but noticeable difference is present at some of the channels. This is only one of the six DOFs were misalignment can be possible and 0.5° should be regarded as small. It is therefore important to be careful when positioning the accelerometers.

Orienting all accelerometers and the input point in a plane is most likely not an optimal arrangement. Also the use of a glue gun gives a short time for adjusting the accelerometer into exactly the right place. The tracks on the cylinders where the accelerometers were mounted much wider than necessary. The accelerometers were first intended to be mounted with plastic clips but the glue was found to be sturdier. Tighter tracks and a design were they are fixed in more DOFs could easily be done, and thus grant a more precise positioning and orientation.

4.5 Substructuring challenges

Several challenges of substructuring has been discussed in this report and they are worth to highlight. One of the simplest, and at the same time the hardest, is to keep track of the orientation at the coupling points. Related to this is that the accelerometers are placed such that they not only describe the motion of the coupling point, but do it in a robust way. But even if this is done, one should be careful when positioning and orientating the accelerometers. The residual states of the experimental model was hard to model but are important to ensure a good fit to test data. To have them slightly separated was essential for numerical stability. Lack of reciprocity at the residual states was also a problem.

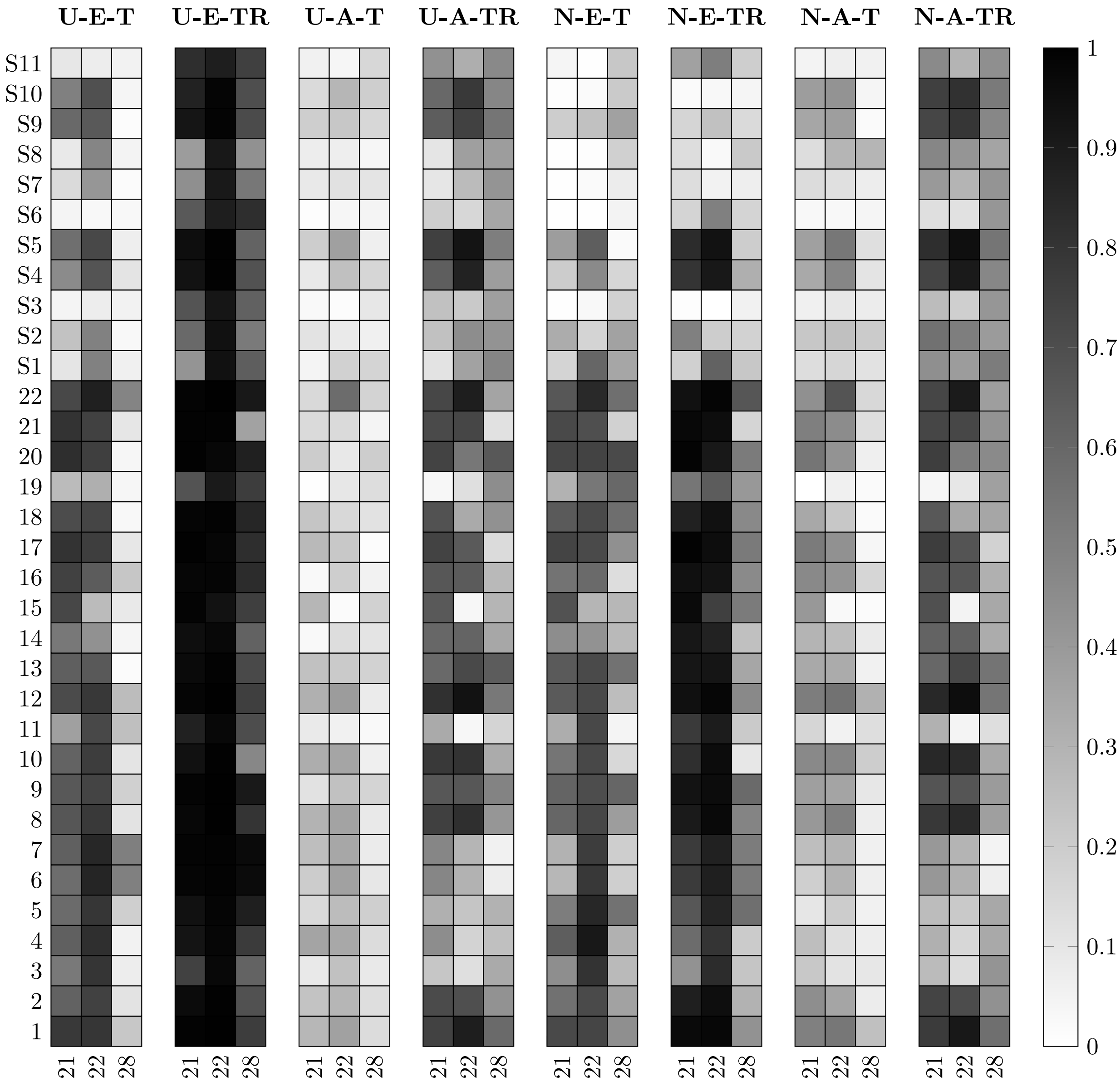

Figure 4.4: *FRAC of the measured coupled system and the coupled state space systems. First is measured BIW coupled with translational DOFs, second coupled with translational and rotational, third is translational coupled FE models and fourth is FE models coupled with both translation and rotation DOFs*

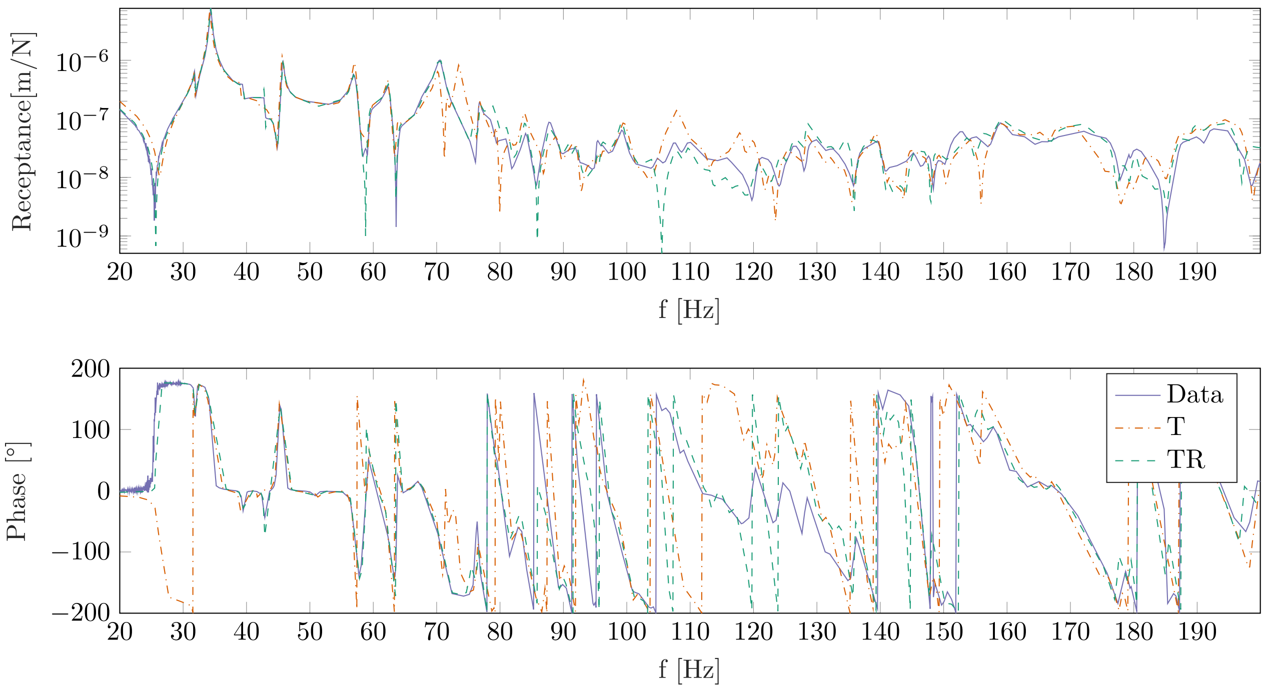

(a) *Experimental BIW model*

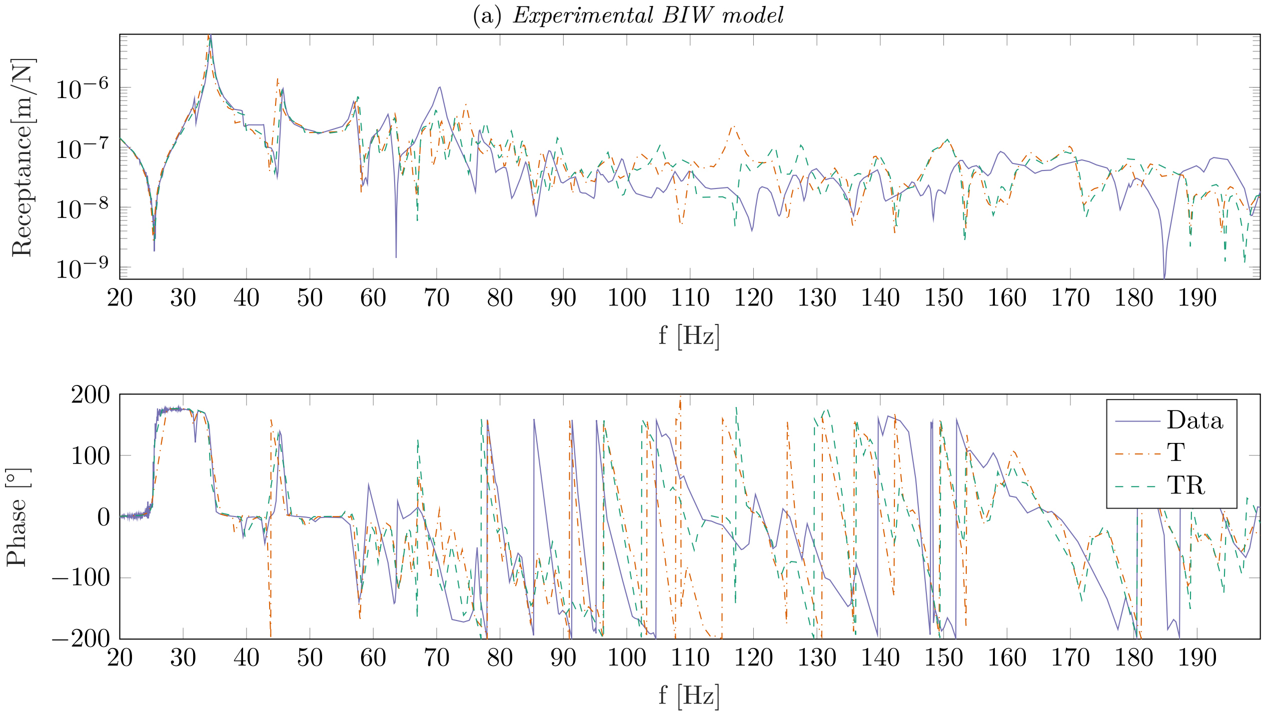

(b) *Analytical BIW model*

Figure 4.5: *Plot of input 22 and output 12 for the coupled BIW and subframe system. T is only coupled with translation DOFs and TR is coupled with both translation rotation*

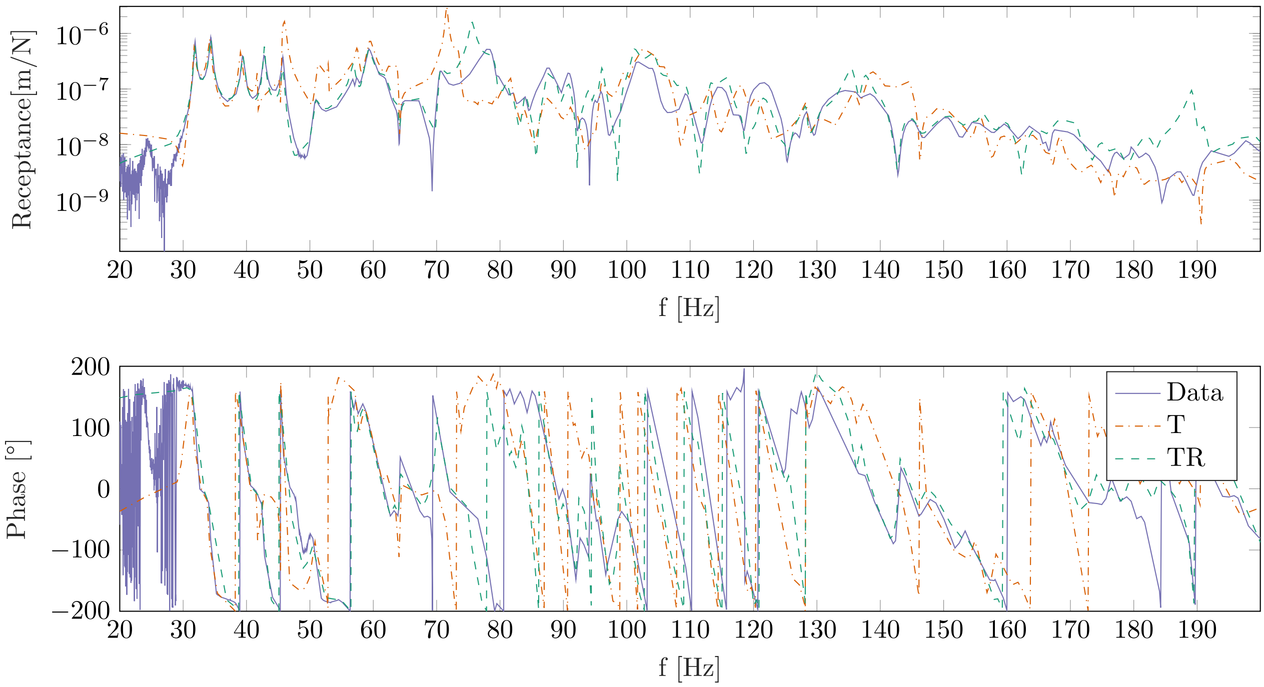

(a) *Experimental BIW model*

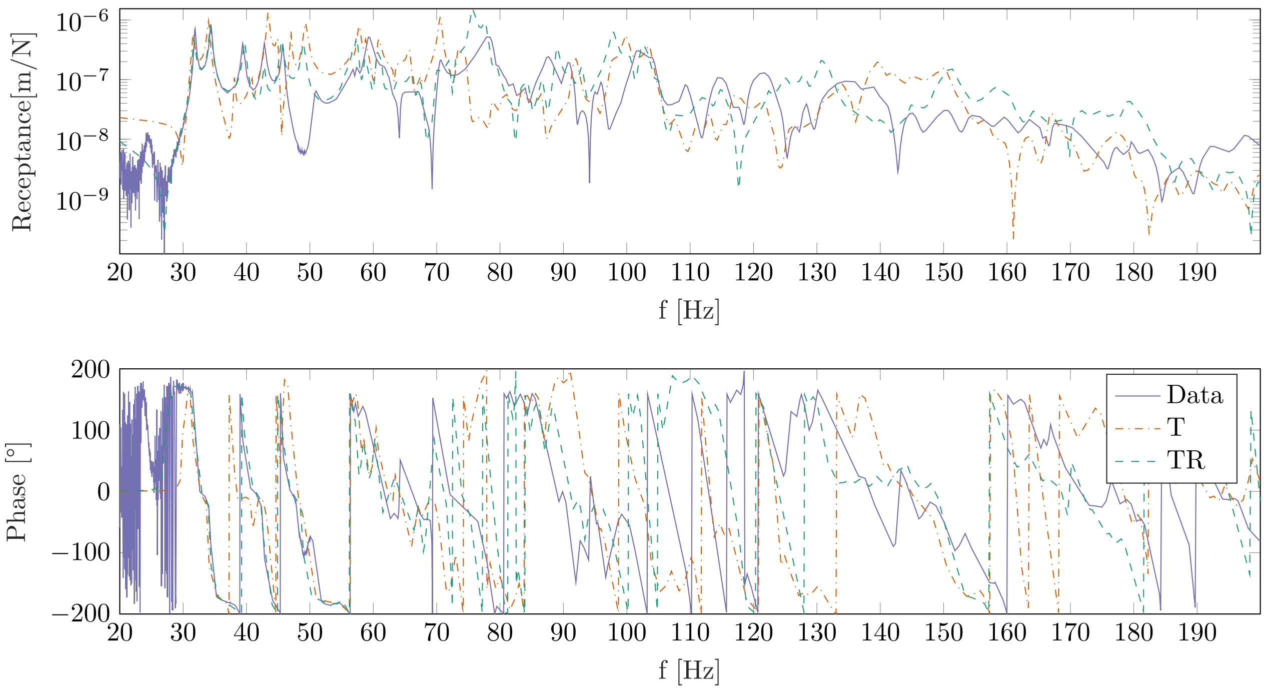

(b) *Analytical BIW model*

Figure 4.6: *Plot of input22 and output 12 for the coupled BIW and subframe system. T is only coupled with translation DOFs and TR is coupled with both translation rotation*

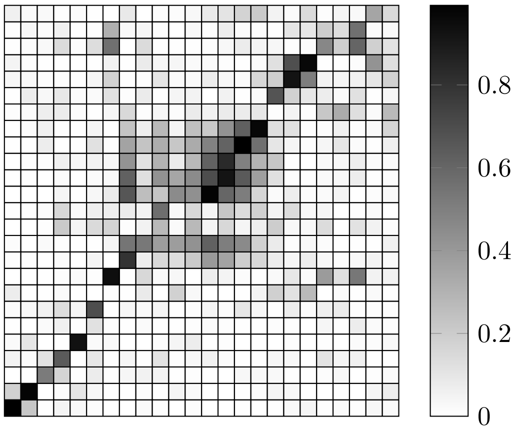

(a) *MAC of the experimental BIW coupled to the updated subframe with translation DOFs*

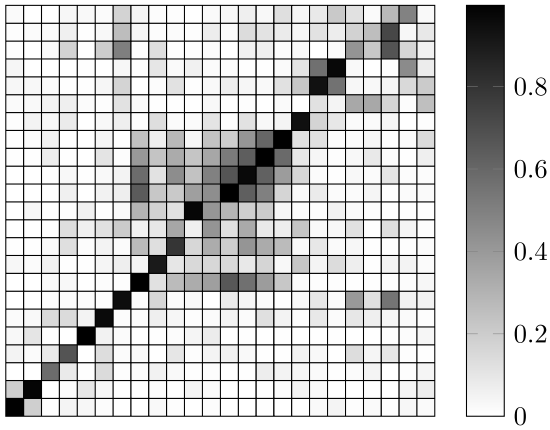

(b) *MAC of the experimental BIW coupled to the updated subframe with translation and rotation DOFs*

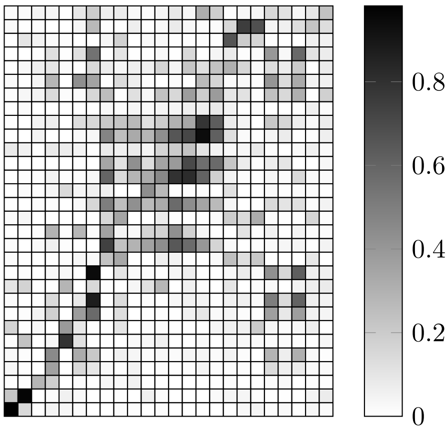

(c) *MAC of the analytical BIW coupled to the updated subframe with translation DOFs*

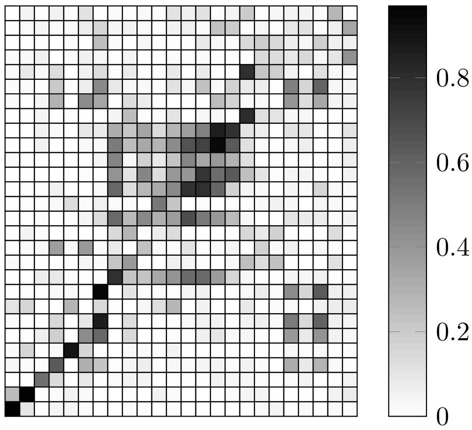

(d) *MAC of the analytical BIW coupled to the updated subframe with translation and rotation DOFs*

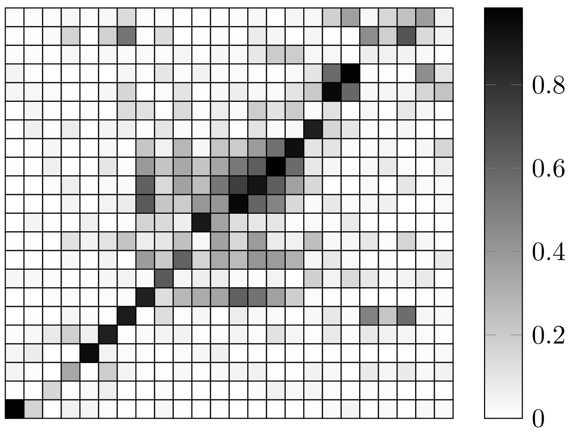

(e) *MAC of the experimental BIW coupled to the nominal subframe with translation and rotation DOFs*

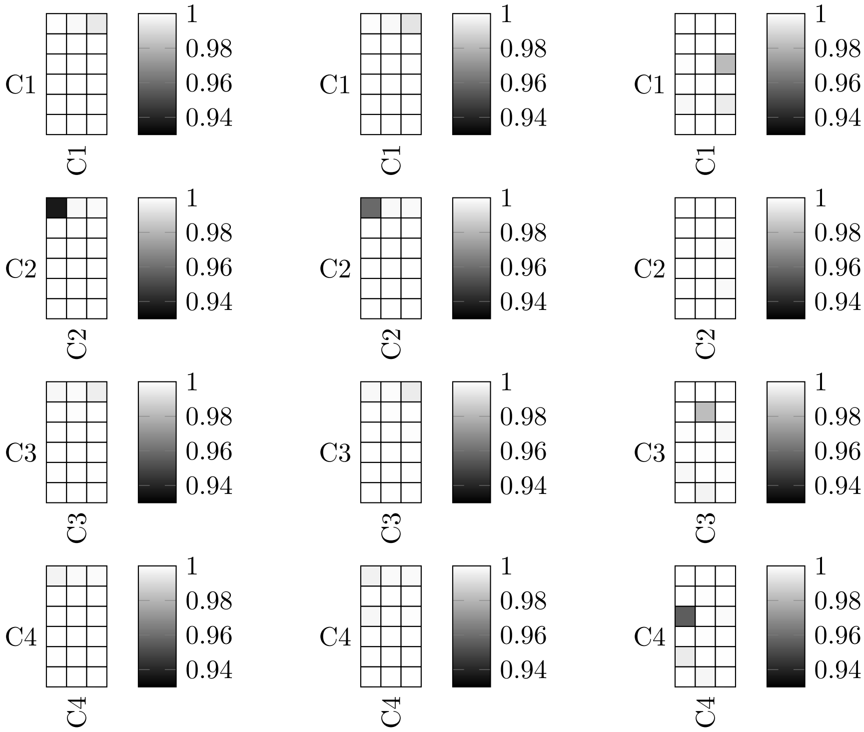

Figure 4.8: *FRAC of direct input output at each cylinder with* $0.5°$ *perturbation in z-direction of sensor placement. First column is sensor one perturbated, second column is second sensor and third column is third sensor.*

5 Conclusion

The proposed coupling method is found to give better results with EMA based models than with FE based models and thus the method fulfills it purpose. A comparison to FRF based coupling would however be interesting as it is a common method within the field of dynamic substructuring.

For strict modal analysis it is highly of the essence to couple both the translational and rotational DOFs, this goes both for EMA and FE based models. If one's focus is on the magnitude of the FRFs it seems to be sufficient to only couple the translational DOFs.

Due to lack of full reciprocity of the used models the rotational inputs used are however not perfect. More inputs from measurements or methods ensuring full reciprocity of the state space models are therefore wanted. Either to obtain more accurate models of the rotational inputs or determine the importance of their accuracy.

To further increase the quality of the model a thorough study of the sensor placements is encouraged. Those used within this project were found to be very sensitive to angular mis-alignment, and no study of translational mis-alignment was done here.

According to the author, the system identification procedure is the most challenging part. That is to ensure that the model fulfills the physical constraints but also fit the measured data. The test data was good but time consuming to gather. It would therefore be interesting to couple state-space models based on chirp or impact data instead.

It is seen that an accurate model of the subframe is important, as the nominal model gives poorer results. The used analytical BIW model is based on nominal data and thus one can expect that it is outperformed by the experimental model.

References

[1] T. Abrahamsson. Modal-parameter extraction for nonproportionally damped linear structures. *International Journal of Analytical and Experimental Modal Analysis* **3** (1988), 62–68.

[2] A. Bylin, M. Gibanica, and T. J. S. Abrahamsson. "Experimental-analytical state-space synthesis of a body-in-white and rear subframe". *Proceedings of the 28th ISMA 2018.* 28th International Conference on Noise and Vibration Engineering, ISMA 2018. Leuwen,Belgium.

[3] R. Craig and A. Kurdila. *Fundamentals of Structural Dynamics.* Wiley, 2006. ISBN: 9780471430445. URL: https://books.google.se/books?id=iP1Er7ULtWwC.

[4] G. Dorendorf. "Variability of nominally identical componenets and their influence in an assembly". MA thesis. 2017.

[5] M. Gibanica and T. J. S. Abrahamsson. *AbraDAQ.* URL: https://github.com/mgcth/abraDAQ (visited on 06/06/2018).

[6] M. Gibanica and T. J. S. Abrahamsson. "Parameter Estimation and Uncertainty Quantification of a Subframe with Mass Loaded Bushings". *Model Validation and Uncertainty Quantification.* Ed. by R. Barthorpe et al. Vol. 3. Cham: Springer International Publishing, 2017, pp. 61–76. ISBN: 978-3-319-54858-6.

[7] M. Gibanica, T. J. S. Abrahamsson, and R. J. Allemang. "Residual states for modal models identified from accelerance data". *Proceedings of the 36th IMAC.* International Modal Analysis Conference. Orlando, FL, USA. In press, 2018.

[8] R. J. Allemang. The Modal Assurance Criterion (MAC): Twenty Years of Use and Abuse. **37** (Jan. 2003).

[9] D. D. Klerk, D. J. Rixen, and S. N. Voormeeren. General Framework for Dynamic Substructuring: History, Review and Classification of Techniques. *AIAA Journal* **46**.5 (May 2008), 1169–1181. DOI: 10.2514/1.33274. URL: https://doi.org/10.2514%5C%2F1.33274.

[10] A. Liljerehn and T. Abrahamsson. "Dynamic sub-structuring with passive state-space components". *Proceedings of the 26th ISMA 2014.* 26th International Conference on Noise and Vibration Engineering, ISMA 2014. Leuwen,Belgium, Sept. 2014.

[11] P. V. Overschee and B. D. Moor. N4SID: Subspace algorithms for the identification of combined deterministic-stochastic systems. *Automatica* **30**.1 (1994). Special issue on statistical signal processing and control, 75–93. ISSN: 0005-1098. DOI: https://doi.org/10.1016/0005-1098(94)90230-5. URL: http://www.sciencedirect.com/science/article/pii/0005109894902305.

[12] Roy R. Craig Jr. and A. J. Kurdila. *Fundamentals of Structural Dynamics.* 2nd Edition. Hoboken, N.J: Wiley, July 11, 2006. 744 pp. ISBN: 978-0-471-43044-5.

[13] P. Sjövall and T. Abrahamsson. Component system identification and state-space model synthesis. *Mechanical Systems and Signal Processing* **21**.7 (2007), 2697–2714. ISSN: 0888-3270. DOI: https://doi.org/10.1016/j.ymssp.2007.03.002. URL: http://www.sciencedirect.com/science/article/pii/S088832700700043X.

[14] M. Van der Seijs et al. An improved methodology for the virtual point transformation of measured frequency response functions in dynamic substructuring (June 2013), 4334–4347.

[15] V. Yaghoubi and T. Abrahamsson. "Automated Modal Analysis Based on Frequency Response Function Estimates". *Topics in Modal Analysis I, Volume 5.* Ed. by R. Allemang et al. New York, NY: Springer New York, 2012, pp. 9–18. ISBN: 978-1-4614-2425-3.

A Figures

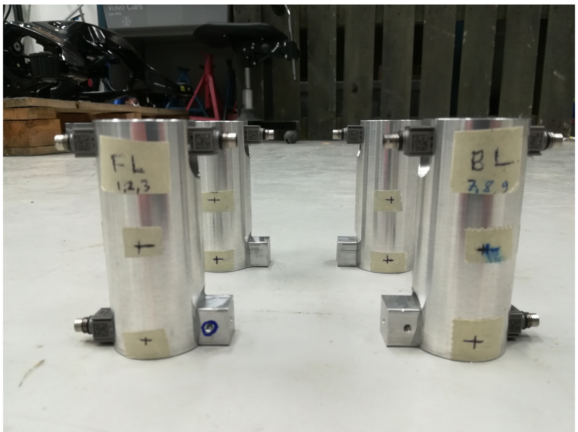

(a) *Coupling cylinders with accelerometers and input cube view 1*

(b) *Coupling cylinders with accelerometers and input cube view 2*

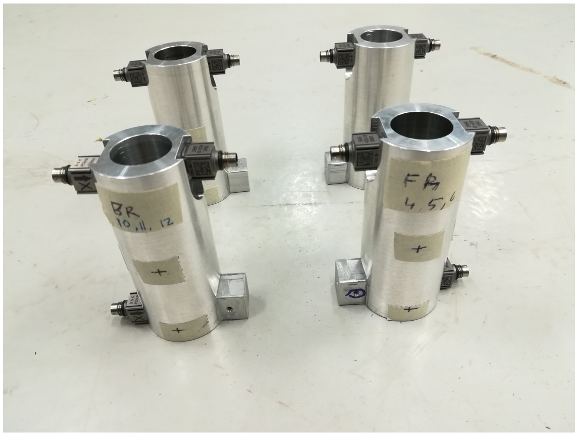

(c) *Coupling cylinders with accelerometers and input cube view 3*

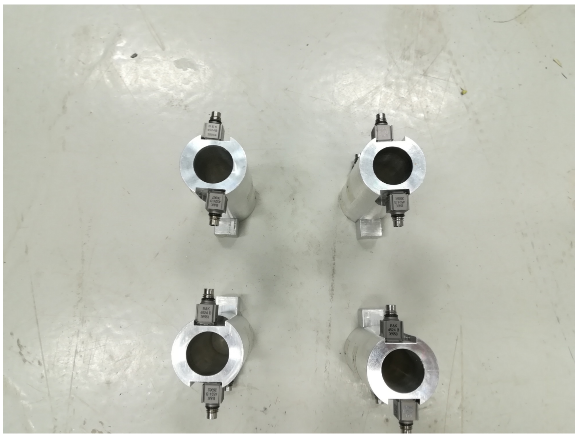

(d) *Coupling cylinders with accelerometers and input cube view 4*

Figure A.1: *Four views of the coupling cylinders*

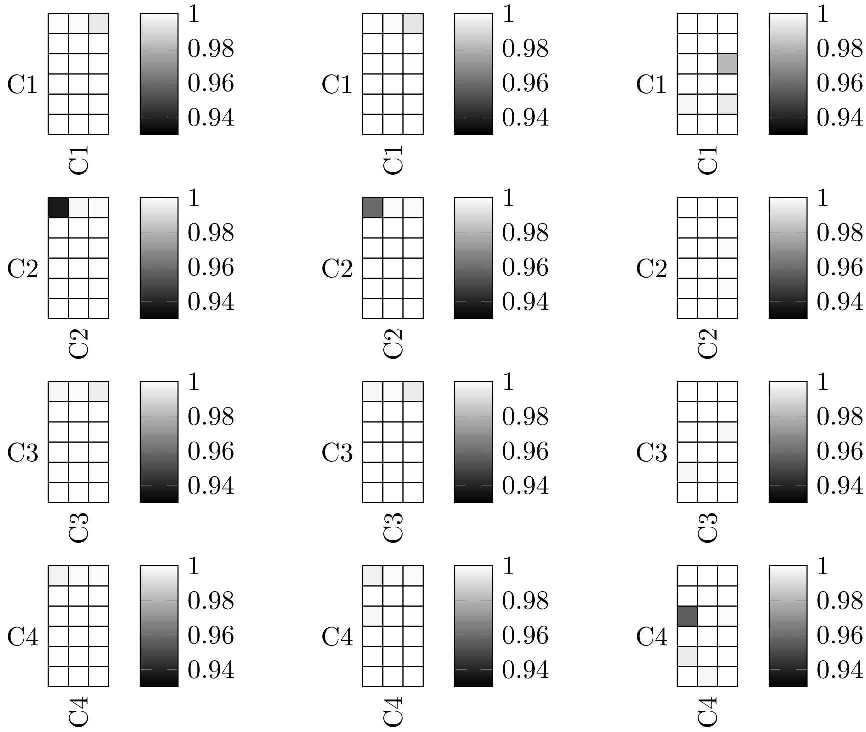

Figure A.2: *FRAC of direct input output at each cylinder with* $0.5°$ *perturbation in z-direction of sensor placement. First column is sensor one perturbated, second column is second sensor and third column is third sensor. The transformation used to transform from the raw test data includes all sensors except for number 7*